

# Limited Elemental Mixing in Nanoparticles Generated by Ultrashort Pulse Laser Ablation of AgCu Bilayer Thin Films in a Liquid Environment: Atomistic Modeling and Experiments

Cheng-Yu Shih,<sup>1,2</sup> Chaobo Chen,<sup>1</sup> Christoph Rehbock,<sup>3</sup> Anna Tymoczko,<sup>3</sup> Ulf Wiedwald,<sup>4</sup> Marius Kamp,<sup>5</sup>  
Ulrich Schuermann,<sup>5</sup> Lorenz Kienle,<sup>5</sup> Stephan Barcikowski,<sup>3</sup> Leonid V. Zhigilei<sup>1,\*</sup>

<sup>1</sup> Department of Materials Science and Engineering, University of Virginia, 395 McCormick Road, Charlottesville, Virginia 22904-4745, USA

<sup>2</sup> Longterm Concept International Pte Ltd, 111 North Bridge Road #18-01, Peninsula Plaza, Singapore, 179098

<sup>3</sup> Technical Chemistry I and Center for Nanointegration Duisburg-Essen (CENIDE), University of Duisburg-Essen, Universitaetsstrasse 5, 45141 Essen, Germany

<sup>4</sup> Faculty of Physics and Center for Nanointegration Duisburg-Essen (CENIDE), University of Duisburg-Essen, Lotharstrasse 1, 47057 Duisburg, Germany

<sup>5</sup> Institute for Materials Science, Synthesis and Real Structure, Kiel University, Kaiserstraße 2, 24143 Kiel, Germany

## Abstract

Pulsed laser ablation in liquids (PLAL) is a promising technique for the generation of colloidal alloy nanoparticles that are of high demand in a broad range of fields, including catalysis, additive manufacturing, and biomedicine. Many of the applications have stringent requirements on the nanoparticle composition and size distributions, which can only be met through innovations in the PLAL technique guided by a clear understanding of the nanoparticle formation mechanisms. In this work, we undertake a combined computational and experimental study of the nanoparticle formation mechanisms in ultrashort PLAL of Ag/Cu and Cu/Ag bilayer thin films. Experimental probing of the composition of individual nanoparticles and predictions from large-scale atomistic simulations provide consistent evidence of limited mixing between the two components from bilayer films by PLAL. The simulated and experimental distributions of nanoparticle compositions exhibit an enhanced abundance of Ag-rich and Cu-rich nanoparticles and a strongly depressed population of well-mixed alloy nanoparticles. The surprising observation that the nanoscale spatial separation of the two components in the bilayer films manifests itself in the sharp departure from the complete quantitative mixing in the colloidal nanoparticles is explained by the complex dynamic interaction between the ablation plume and liquid environment revealed in the simulations

---

\* Corresponding Author, E-mail: lz2n@virginia.edu.

of the initial stage of the ablation process. The simulations predict that rapid deceleration of the ablation plume by the liquid environment results in the formation of a transient hot and dense metal region at the front of the plume, which hampers the mixing of the two components and, at the same time, contributes to the stratification of the plume in the emerging cavitation bubble. As a result, nanoparticles of different sizes and compositions are produced in different parts of the emerging cavitation bubble during the first nanoseconds of the ablation process. Notably, the diameters of the largest nanoparticles generated in the simulations of the initial stage of the ablation process are more than twice larger than the thickness of the original bilayer films, which provides a plausible scenario for the formation of large nanoparticles observed in the experiments. The conclusion on limited elemental mixing in the nanoparticles is validated in simulations of bilayers with different spatial order of Cu and Ag layers, even though the two systems exhibit some notable quantitative differences mainly related to the different strength of electron-phonon coupling in Cu and Ag. Overall, the results of this study provide new insights into the formation mechanism of bimetallic nanoparticles in ultrashort PLAL from thin bilayer targets and suggest that the formation of alloy nanoparticles from immiscible elements may be hampered for targets featuring distinctive elemental segregation.

## 1. Introduction

Pulsed laser ablation in liquids (PLAL) is a promising technique for the generation of colloidal alloy nanoparticles that are of high demand in a broad range of fields, including catalysis<sup>1,2</sup> and biomedicine.<sup>3</sup> In this context, the AgCu system is of particular interest as both constituents possess high relevance as antimicrobial agents<sup>4,5</sup> as well as in electro- and photocatalysis.<sup>6,7</sup> Furthermore, the AgCu system is interesting for fundamental studies of elemental miscibility on the nanoscale as its bulk phase diagram is relatively simple and shows a large miscibility gap (elemental segregation).<sup>8</sup> On the other hand, the relatively low oxidation susceptibility of the constituents, in contrast to other 3d and 4d transition metals, makes it easier to experimentally study elemental mixing independently of oxidation. Moreover, it has been shown that electron transfer from Cu to Ag within the alloy nanoparticles results in far better resistance to oxidation as compared to pure Cu nanoparticles.<sup>9</sup>

Many of the applications of alloy nanoparticles impose stringent requirements on the nanoparticle compositions and size distributions, thus presenting a challenge for the development of advanced methods capable of fine control over the characteristics of nanoparticles. The size and composition of nanoparticles synthesized by PLAL can be affected by the choice of irradiation conditions (laser pulse duration and fluence)<sup>10-12</sup> as well as the liquid medium.<sup>13</sup> For example, a strong effect of oxidative properties of solvent on the phase arrangement in nanoparticles produced by PLAL has recently been demonstrated for a bimetallic FeAu system, where core-shell nanoparticles with a gold core and an iron oxide shell are observed in water, while a zero-valent iron core and a gold shell nanoparticles are produced by ablation in organic solvents like acetone or methyl methacrylate.<sup>14</sup> Another approach to the size and composition control is the introduction of surface-active species into the liquid environment like surfactants<sup>15,16</sup> or electrolytes,<sup>17-19</sup> which induce a size quenching effect and may alter particle composition and degree of oxidation.<sup>20</sup>

Recently, the design of target materials for the PLAL synthesis of alloy nanoparticles has been the focus of attention, going from commonly used alloy targets either towards pressed mixed powder targets to improve synthesis variability<sup>1,21,22</sup> or towards thin films and multilayer targets.<sup>12,23,24</sup> The use of thin films and multilayers adds an additional degree of freedom to the experimental setup and enables more precise control over the laser energy deposition and atomic mixing that defines the composition of the nanoparticles. In particular, the thin layer PLAL makes it possible to ensure that a well-defined target depth, set by the layer thickness, is ablated in a single pulse experiment. As a result, PLAL of thin films not only allows for the exploration of the target thickness effects,<sup>25,26</sup> but also sets the ratio of two elements being ablated in a single pulse, simply by varying the layer thickness of each element in a bilayer or multilayer film, even for immiscible or partly miscible elements. The experiments with thin bilayer targets also enable investigation of the possible role the layer sequence may play in defining the structure and composition of the formed nanoparticles<sup>23</sup> or analysis of the influence of phase boundaries and layer arrangements in bilayer, multilayer, and non-segregated binary alloy targets. For example,

it has recently been demonstrated that nanosecond PLAL of AuFe thin films can produce an exceptionally high FeAu core-shell nanoparticle yield reaching 99.7%, and that alloy and multilayer thin film targets provide higher yields as compared to the bilayer thin films.<sup>12</sup> Interestingly, in the same experimental series but with ultrashort PLAL of Au/Fe and Fe/Au bilayer thin films in acetone, a significantly higher core-shell yield was observed when iron was the top layer of the bilayer film.

The large number of experimental parameters and the complexity of processes involved in the formation of alloy nanoparticles in PLAL make the task of designing experimental setups for improved control over the nanoparticle size and composition challenging. The progress in the fundamental understanding of the PLAL mechanisms can be most efficiently achieved through a combined experimental and computational investigation of various factors affecting the nanoparticle generation, which is an approach that has not been applied to alloy nanoparticle formation to date.

Experimentally, metal alloy nanoparticles from multiple elements have been synthesized by PLAL, which includes bimetallic nanoparticles composed of components exhibiting different levels of solid-state miscibility according to bulk phase diagrams. For alloys with unlimited solid-state miscibility in the bulk, such as AgAu<sup>21</sup> and PtIr,<sup>27</sup> the nanoparticles produced by PLAL are found to exhibit elemental solid solution mixing on a single particle level.<sup>21</sup> Moreover, the alloy nanoparticles synthesized from partially immiscible elemental components, such as AuPt<sup>22,28</sup> or AuFe,<sup>29-31</sup> are also often found to have a metastable solid solution structure rather than a phase segregated state predicted by bulk phase diagrams at room temperature. In particular, for AuFe, small particle diameters and gold-rich compositions were identified as clear determinators favoring solid solution over segregated core-shell morphologies.<sup>32</sup> Further studies reveal that the degree of mixing in the target and the pulse duration both significantly influence the nanostructure of the PLAL-fabricated nanoparticles. In the AuFe system, a well-mixed target in combination with nanosecond pulse durations primarily yielded a high fraction of core-shell structures, which are predicted to be energetically preferable by free surface energy calculations. A smaller fraction of such particles, however, was generated when targets with inadequate mixing were used and the irradiation by ultrashort pulses was applied.<sup>12</sup>

The AgCu system is another example of an eutectic system with a very limited mutual solubility in the solid-state, which presents a scientifically interesting and practically important case study for the nanoparticle synthesis. To our knowledge, there have only been a few studies dedicated to the generation of AgCu bimetallic nanoparticles by PLAL.<sup>33-36</sup> The results of a detailed investigation of AgCu nanoparticles produced by nanosecond PLAL in an aqueous solution of 0.02 M polyvinylpyrrolidone as a capping agent is reported in Ref. 33. The bulk alloy targets used in these experiments have different compositions and eutectic microstructure featuring sub-micrometer thickness of the copper- and silver-rich layers. The synthesized nanoparticles are characterized by biphasic morphology for silver-rich targets, whereas the formation of silver-rich shell – copper-

rich core structures is observed for copper-rich targets. At intermediate compositions, on the other hand, the nanoparticles are featuring well-mixed structures with evidence of nanoscale phase separation. Based on these findings, the authors developed a simple thermodynamic model to explain the dependence of the observed structures on the nanoparticle size and overall composition.<sup>33</sup> A follow up thermodynamic analysis predicted a metastable solid solution state for small AgCu nanoparticles, where the demixing into the core-shell structure occurs but does not result in the formation of a well-defined phase boundary.<sup>37</sup> These findings were complemented by analysis of structural transformations in laser-generated AgCu nanoparticles upon heating, where the initial nanocrystalline solid solution structures are observed to evolve into two-phase structures with a Janus morphology.<sup>35</sup> Similarly, the metastable nature of laser-generated core-shell AuFe nanoparticles has also been evidenced by the results of *in situ* transmission electron microscopy (TEM) heating experiments reported in Ref. 38. The model suggested in Ref. 33 was validated and mathematically refined for the AuFe system, showing how FeAu core-shell formation is driven by the interface energy minimization.<sup>12</sup> In addition to the direct synthesis of bimetallic nanoparticles by PLAL of two-component targets with different degrees of phase separation, other techniques, such as nanosecond ablation of Cu targets into a colloidal solution of Ag nanoparticles, yielding core-shell morphologies with a Ag core and a Cu shell,<sup>34</sup> as well as a combination of plasma treatment of Cu and Ag micropowder suspension in ethanol with nanosecond laser irradiation, leading to the formation of well-alloyed nanoparticles.<sup>36</sup>

Theoretical and computational studies of PLAL have been focused on analysis of the general effects of the liquid environment on the ablation dynamics<sup>39-42</sup> and the mechanisms of the nanoparticle formation.<sup>43-48</sup> In particular, large-scale atomistic simulations of ultrashort PLAL<sup>40,45,46</sup> have revealed two distinct mechanisms of the nanoparticle formation in PLAL, the rapid nucleation and growth of small nanoparticles in the metal-liquid mixing region and the generation of larger droplets through the breakup of a transient hot metal layer formed at the interface of the liquid environment, yielding nanoparticles of two different size ranges at the early stage of the ablation process. These computational predictions provide a plausible explanation for the bimodal character of nanoparticle size distributions commonly observed in the ultrashort PLAL experiments,<sup>11,46,49</sup> and are supported by the results of time-resolved imaging<sup>46</sup> and X-ray probing<sup>50</sup> of the expanding cavitation bubble. Moreover, the atomistic simulations have provided important insights into the effect of the pulse duration,<sup>47</sup> target geometry (thin films<sup>45</sup> vs. bulk targets<sup>40</sup>), and spatial modulation of the laser energy deposition<sup>51</sup> on the nanoparticle generation mechanisms. All these studies, however, have been done for single-component targets, and the processes controlling the composition of alloy nanoparticles have not been addressed in the simulations of PLAL so far.

In this paper, we report the results of the first combined computational and experimental study focused on the ability of the ultrashort PLAL to produce alloy nanoparticles with compositions matching that of the target

material. The choice of the target, a thin bilayer film consisting of Ag and Cu layers deposited on a glass substrate, makes it possible to not only control the average composition of the target, but to ensure that this composition also characterizes the total ablation plume, as the whole film is removed from the target by a single laser shot. The use of the Ag-Cu bilayer as a target also brings about an additional interesting effect related to the much stronger electron-phonon coupling in Cu as compared to Ag. As has been demonstrated in a recent study of laser irradiation of Ag-Cu bilayers in air,<sup>52</sup> the difference in the strength of the electron-phonon coupling results in the channeling of the deposited laser energy to the Cu layer, leading to the sensitivity of laser nano-structuring of the bilayer to the order in which the two layers are deposited to the substrate. To check the possible implications of this effect on the nanoparticle generation in PLAL, in the present study we perform simulations and experiments for both Cu-top and Ag-top bilayer targets. In contrast to the earlier experimental studies of nanosecond PLAL of bilayer targets,<sup>12,23,24</sup> we utilize ultrashort laser pulses and focus our attention on the degree of compositional uniformity that can be achieved by the laser ablation in liquids. The analysis of the nanoparticle size and composition distributions, as well as the correlation between the size and composition, is performed in both simulations and experiments. The lateral separation of sequential irradiated spots assures single-pulse conditions in the experiments, which helps with establishing direct links to the results of single pulse PLAL simulations. The implications of the fast, dynamic processes occurring during the first nanoseconds of the ablation process on the final characteristics of the nanoparticles are discussed based on the computational results and experimental observations.

## **2. Methods**

In this section, we describe the computational model and experimental setup used in the investigation of the mechanisms of nanoparticle formation by ultrashort pulse laser ablation of a bilayer AgCu thin film in a liquid environment. The focus of the modeling and experimental efforts is on the composition of the colloidal nanoparticles generated by PLAL and, in particular, on any deviations of the nanoparticle composition from the nominal composition of the bilayer target. The composition of the nanoparticles, therefore, is thoroughly characterized in experiments and explained based on the dynamic picture of the ablation process revealed in the simulations.

### **2.1. Computational model**

The simulations of laser ablation of Ag/Cu bilayer metal films in water environment are performed with a computational model combining a fully atomistic description of laser interaction with metal targets,<sup>40,53-55</sup> a coarse-grained representation of liquid,<sup>45,56,57</sup> and acoustic impedance matching boundary conditions<sup>58</sup> designed to mimic the nonreflecting propagation of the laser-induced pressure waves through the boundaries of the

computational domain. A schematic representation of the initial system and computational setup used in the simulations is shown in Figure 1 and is briefly described below.

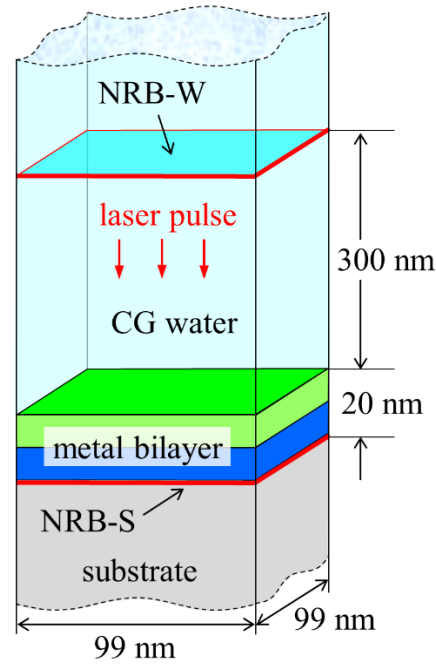


**Figure 1.** Schematic representation of the initial system used in simulations of short pulse laser interaction with a 20-nm-thick metal bilayer film in water. The film consisting of two metal layers (shown by green and blue colors) is deposited on a transparent silica substrate (bottom grey region) and is irradiated through water. The laser interaction with metal bilayer is simulated with atomistic TTM-MD model accounting for the laser energy deposition, electron-phonon equilibration, and electronic heat transfer within the general framework of classical MD method. Two configurations, with Cu on top of Ag and Ag on top of Cu, are considered in the simulations. A 300-nm-thick layer of water adjacent to the metal bilayer is represented by the coarse-grained MD model (CG water). The elastic response of the silica substrate and non-reflecting propagation of the laser-induced pressure wave from the CG water to the overlaying part of the water environment are represented by acoustic impedance matching boundary conditions applied at the substrate-film interface (NRB-S) and at the top of the coarse-grained MD part of the system (NRB-W). These boundary conditions mimic the response of semi-infinite substrate and water environment to the laser-generated pressure waves. In the lateral directions, parallel to the irradiated surface, the dimensions of the computational cell are  $98.7 \times 98.7 \text{ nm}^2$  and periodic boundary conditions are applied.

The laser interaction with metal bilayers is simulated with a hybrid atomistic-continuum model that combines molecular dynamics (MD) method with a continuum description of laser excitation of conduction band electrons followed by electron-phonon equilibration based on two-temperature model (TTM).<sup>59</sup> Since the combined TTM-MD model has been described in detail in previous publications,<sup>40,53-55</sup> here we only provide parameters of the computational setup specific for the simulations reported in this paper.

The simulations are performed for bilayer configurations consisting of two 10-nm-thick layers of Cu and Ag. Two configurations are considered in the simulations, one where the top layer facing the water is Cu and another where the top layer is Ag, within the manuscript consecutively abbreviated as glass/Ag/Cu and glass/Cu/Ag, respectively. The interatomic interactions in the MD part of the TTM-MD model are described by the embedded atom method (EAM) potential with parametrization suggested by Williams *et al.*<sup>60</sup> This potential

is fitted to experimental values of cohesive energy, elastic constants, energies of crystal defects (vacancies, interstitials, stacking faults), vibrational properties, surface energies, thermal expansion of pure components, as well as the energies of several imaginary Cu-Ag compounds predicted in density functional theory (DFT) calculations. The potential provides a reasonable description of the eutectic phase diagram of Cu-Ag alloy, with the calculated melting temperatures of pure component (1327 K for Cu and 1267 K for Ag) within 3% of the experimental values and the eutectic temperature (935 K) 11% below the experimental value.<sup>60</sup> To further probe the performance of the potential at higher temperatures relevant to the simulations of laser ablation, we evaluated the temperature dependence of surface tension using the test area method<sup>61</sup> and determined the critical temperature as a temperature at which the surface tension vanishes.<sup>62</sup> This yields the thermodynamic critical temperatures of 5368 K and 6350 K for Ag and Cu, respectively. These critical temperatures are within the ranges of experimental values reported for the two metals.<sup>63</sup>

The silica substrate is not represented with atomic resolution but introduced through a non-reflecting boundary condition (NRB-S in Figure 1) parametrized to account for the displacement of the metal-substrate interface in response to the laser-induced phase transformations and expansion of the metal bilayer. This dynamic acoustic impedance matching boundary condition is implemented as an imaginary plane that interacts with the metal atoms through the Lennard-Jones (LJ) potential defined as a function of the distance between a metal atom and the imaginary plane, as described in detail in Ref. 58. The parameters of the LJ potential are fitted to reproduce the experimental values of the work of adhesion between the metal films and silica overlayer<sup>64</sup> as well as the local stiffness under uniaxial compression,<sup>52,58</sup> yielding the following LJ length and energy parameters:  $\sigma_{\text{Ag-S}} = 2.96 \text{ \AA}$ ,  $\epsilon_{\text{Ag-S}} = 230 \text{ meV}$  for Ag – substrate interaction and  $\sigma_{\text{Cu-S}} = 4.62 \text{ \AA}$ ,  $\epsilon_{\text{Cu-S}} = 270 \text{ meV}$  for Cu – substrate interaction. These parameters are close to the ones obtained for the Cu/Ag – silica interface in Ref. 52, where a similar fitting procedure was used, but the interatomic interactions in Cu and Ag were described with a different parametrization of the EAM potential. The application of the NRB-S boundary condition eliminates the need to model the substrate with atomic resolution, and still enables a realistic description of the transformation of a part of the energy deposited by the laser pulse into the energy of a pressure wave generated in the substrate.

The description of the electron and lattice temperature dependences of the electron–phonon coupling factor and electron heat conductivity of Ag and Cu included in the TTM equations accounts for the thermal excitation from the electron states below the Fermi level.<sup>65</sup> The temperature dependence of the electron thermal conductivity is described by the Drude model relation fitted to the experimental values of thermal conductivity of solid Cu and Ag at the melting temperature.<sup>66</sup> The properties of the mixed region are approximated by the average of the properties of Cu and Ag weighted by the atomic ratio.

The energy deposition by a 100 fs laser pulse is simulated through a source term added to the TTM equation for the electron temperature. The source term simulates the excitation of the conduction-band electrons

by a laser pulse with a Gaussian temporal profile and reproduces the exponential attenuation of laser intensity with depth under the surface (Beer–Lambert law).<sup>53,67,68</sup> The values of the optical penetration depth at a laser wavelength of 800 nm, 12 nm and 13 nm for Ag and Cu, respectively,<sup>69,70</sup> are assumed in the simulations. Since the electron temperature equilibration throughout the thickness of the 20-nm bilayer takes place within the first picosecond after the laser pulse,<sup>71</sup> we do not include the energy transport by non-thermal (ballistic) electrons<sup>66,72,73</sup> into the description of the laser energy deposition. The implementation of the source term is based on a cell-by-cell attenuation of the laser light to allow for the laser energy deposition to the films consisting of two metal layers with slightly different absorption properties. To account for the finite transmission of the laser light through the 20-nm-thick bilayer, the source term is modified<sup>67,68</sup> so that the full amount of energy defined by the absorbed laser fluence  $F_{abs}$  is deposited in the bilayer. The value of the absorbed laser fluence,  $F_{abs} = 100$  mJ/cm<sup>2</sup>, is chosen to be more than three times higher than the threshold fluence for the onset of phase explosion (explosive decomposition of superheated molten metal into vapor, small atomic clusters, and droplets) in PLAL of a 20-nm-thick Ag film.<sup>45</sup> As discussed in Section 2.3, the ablation regime in the simulations is comparable to the experiments in this study.

The liquid environment is represented by a combination of a coarse-grained (CG) MD model<sup>56,45</sup> used in the vicinity of the irradiated target with a non-reflecting boundary condition<sup>58</sup> (NRB-W in Figure 1) parametrized to simulate a non-reflecting propagation of pressure wave generated by laser ablation of the bilayer film from the CG water region into the overlaying semi-infinite water environment. In the CG MD model, each particle represents several water molecules, and the degrees of freedom missing in such CG representation are accounted for through a heat bath approach that associates an internal energy variable with each CG particle.<sup>45,56,57</sup> The energy exchange between the internal (implicit) and dynamic (explicit) degrees of freedom are controlled by the dynamic coupling between the translational degrees of freedom and the radial (breathing) mode associated with each coarse-grained particle, as described in detail in Refs. 45,56,57. The capacity of the internal heat bath associated with each CG particle, its mass, and the parameters of interparticle interaction are chosen so that the CG model exactly reproduces the density and heat capacity of water, while other properties relevant to the simulation of laser ablation in water, such as the speed of sound, bulk modulus, viscosity, surface energy, melting temperature, critical temperature, and critical density, do not deviate from the experimental values by more than 25%.<sup>45,56</sup> The cross-interaction between metal atoms and the CG water particles is described by LJ potential with the following length and energy parameters:  $\sigma_{Ag-CG} = 2.49$  Å,  $\epsilon_{Ag-CG} = 49$  meV for Ag – CG water interaction and  $\sigma_{Cu-CG} = 2.07$  Å,  $\epsilon_{Cu-CG} = 53$  meV for Cu – CG water interaction. The values of  $\sigma$  are based on Cu-water and Ag-water equilibrium distances predicted in DFT calculations,<sup>74,75</sup> while  $\epsilon$  is chosen based on the values of surface<sup>60</sup> and interfacial energies for the two metals and water, so that the experimental observations of complete spreading of water on chemically clean Cu and Ag surfaces<sup>76-78</sup> are reproduced by the model. Overall, the

combination of CG MD model with NRB-W enables us to reproduce the effect of the water environment with reasonable accuracy and at a manageable computational cost.

The dimensions of the computational domain in the lateral directions, parallel to the irradiated surface, are  $98.7 \times 98.7 \text{ nm}^2$ , and periodic boundary conditions are applied in these directions, as shown in Figure 1. With the 10 nm thickness of Cu and Ag layers, the computational system consists of 8.29 million Cu and 5.76 million Ag atoms. The choice of the lateral size of the computational system is defined by an assumption that the characteristic length-scale of processes responsible for the nanoparticle generation in the explosive decomposition of the 20-nm-thick bilayer is much smaller than 100 nm, and these processes should not be affected by any artifacts introduced by the periodic boundary conditions. One of the surprising computational predictions (supported by the experimental observations), however, is that the diameters of the largest nanoparticles produced by the laser ablation in water are substantially larger than the film thickness, and the periodic boundary conditions still have some effect on the formation of such nanoparticles (see Section 3.3). The thickness of the layer of water represented by the CG MD model, 300 nm, is chosen to include the water region brought to the supercritical state and undergoing vaporization due to the direct interaction with the hot metal ablation plume. This layer consists of 36.3 million CG particles. The systems used in the simulations and illustrated in Figure 1 are thoroughly equilibrated at 300 K before applying laser irradiation.

## 2.2. *Experimental setup*

The experimental component of the present study is motivated by the computational predictions, although there are some differences between the computational and experimental setups, as discussed below, in Section 2.3. The glass/Ag/Cu and glass/Cu/Ag bilayer targets used in the experimental part of this study were prepared from elemental Ag and Cu targets by pulsed laser deposition (PLD) in UHV conditions at ambient temperature using a ns KrF excimer laser (248 nm) at a repetition rate of 10 Hz. The experimental setup has been described in more detail elsewhere.<sup>79</sup> Ag and Cu films were deposited at a laser fluence of  $16 \text{ J cm}^{-2}$  resulting in deposition rates of  $3.2 \text{ nm min}^{-1}$  for Ag and  $1.1 \text{ nm min}^{-1}$  for Cu on glass substrates at 50 mm distance between targets and substrate.

Laser ablation of AgCu targets was performed in HPLC grade acetone with purity >99.9% from Sigma-Aldrich, adapting a previously described procedure<sup>12,23</sup> with 10 ps, 1064 nm pulses of an Nd:YAG laser with a pulse energy of 88.5  $\mu\text{J}$  and an incident fluence of  $3.8 \text{ J/cm}^2$  at a repetition rate of 100 kHz. The film targets were placed in acetone, at the bottom of a glassy batch-chamber, and ablated from the top. The focal point was moved for each subsequent laser pulse with velocity of 5 m/s in order to ablate a different part of the film at each single laser pulse. This leads to a minimum distance of 50  $\mu\text{m}$  between the ablation spots, which is similar to the diameter of the ablation spots. Hence, overlaps between the spots can be considered to be negligible. Please note that in

the experimental section the incident fluence is given, which is substantially higher than the absorbed fluence used in the discussion of the simulations.

The chemical composition and diameters of individual nanoparticles are analyzed by bright-field TEM and energy dispersive X-ray (EDX) spectroscopy on a Tecnai F30 STWIN G2 with 300 kV acceleration voltage equipped with a Si/Li detector (EDAX System). The colloidal samples were dispersed on nickel TEM grids with a lacey carbon carrier film (Plano GmbH). Therefore, nickel and carbon signals are not included in the quantification of the nanoparticle chemical composition.

Analysis of the targets by SEM and EDX was conducted with a Philips XL 30 (XL Series) and a Zeiss Leo 1530 at an anode voltage of 20 kV. The thicknesses of the deposited Ag and Cu layers were analyzed by EDX spectroscopy using an Oxford instruments (detector) XMAX 80 $\mu\text{m}^2$  setup with ThinFilmID software (version 1.3.0). This software allows the calculation of the deposited thicknesses using the layer sequence and a semi-infinite substrate (glass) assuming the volumetric element densities of each layer. The ablation spots were analyzed with an Apreo S LoVac SEM (Imaging conditions: 5 kV, 0.1 nA), and EDS line scans were conducted with a Thermo Fisher Scientific EDS System (Thermo Scientific UltraDry silicon drift X-ray detector). For measurement, the sample was mounted onto the aluminum stub by adhesive carbon tape.

### **2.3. *Connection between simulated and experimental conditions***

Before turning to the discussion of the computational predictions and experimental observations, we note that the goal of the simulations is not to reproduce the exact experimental conditions but to provide insights into the mechanisms of the nanoparticle formation at the initial highly-nonequilibrium dynamic stage of the ablation process. There is no one-to-one correspondence between the simulated systems and those used in the experiments, which is mostly explained by the way this collaborative project evolved. The simulations were performed first and stimulated the experimental investigation of similar systems. The 20 nm bilayer films studied in the simulations, however, were too thin for reliable uniform film deposition, and the film thickness was increased to  $\sim 80$  nm in experiments. The pulse duration was also increased from 100 fs to 10 ps to minimize the beam interaction with the liquid environment, which was also changed from water to acetone to minimize the oxidation of nanoparticles. The possible implications of the differences in the parameters of the computational and experimental setups are briefly discussed below.

In both modeling and experiments, the targets are CuAg bilayer films deposited on a glass substrate. The total thickness of the films are about four times smaller in the simulations as compared to experiments, 20 nm (10 nm Ag and 10 nm Cu layers) in simulations, and  $\sim 80$  nm in the experiments (see Section 3.4). All films, however, are sufficiently thin to ensure that a uniform distribution of the electron temperature is established throughout the film thickness prior to the electron-phonon equilibration. Thus, while the absorbed laser fluence required for the

onset of the phase explosion is likely to be about four times higher in the experiments, the ablation process itself can be expected to be similar. Moreover, since one of the main goals of the simulations is to establish whether the composition of nanoparticles exhibit any deviation from the average composition of the bilayers, the thinner films considered in the simulations put the conditions for any compositional variation in the nanoparticles to a more stringent test. That is, if the nanoscale separation of the two components in the simulated 20-nm-thick bilayer could cause the compositional variation in the nanoparticles generated by laser ablation, then this effect can be expected to be amplified for a thicker ~80 nm bilayer considered in the experiments.

The irradiation conditions used in the simulations and experiments are also comparable. In the simulations, the absorbed fluence is more than three times above the threshold fluence for the onset of the phase explosion in a 20-nm-thick Ag film,<sup>45</sup> and about 10 times above the fluence threshold for complete melting of the 20-nm-thick bilayer Ag/Cu. In experiments, the incident fluence was set to 3.8 J/cm<sup>2</sup>, which is about 2-4 times above the threshold fluence determined from single-shot ablation of a bulk silver target in water and isopropanol at the utilized pulse duration of 10 ps.<sup>80</sup> Based on this we can assume complete film evaporation in the central part of the laser spot focused on a ~80-nm-thick Ag/Cu bilayer. The pulse durations of 100 fs (simulations) and 10 ps (experiments) are both in the ultrashort domain, where the conditions of both thermal and stress confinement are realized.<sup>54,81-83</sup> Recent simulations<sup>47</sup> suggest that the transition from ultrashort to short (hundreds of picoseconds to nanoseconds) laser pulses can lead to substantial changes in the nanoparticle formation mechanisms in PLAL, while the variation of the laser pulse duration within the ultrashort range (femtoseconds to tens of picoseconds) does not lead to qualitative changes in the ablation dynamics.

Finally, the CG MD model of the liquid environment is parametrized for water, while the experiments are done in acetone. The properties of the liquid environment are playing an important role in defining the lifetime, shape, and the maximum size of the cavitation bubble,<sup>84,85</sup> ablation threshold and target surface modification in multi-pulse irradiation regime,<sup>86</sup> as well as the shape, size, and composition of the nanoparticles.<sup>13,84,87,88</sup> Furthermore, the chemical reactivity of water and acetone is quite different, so that PLAL of Cu in water yields copper oxides, whereas the same process in acetone yields elemental copper covered with a graphitic layer.<sup>89</sup> Note that for PLAL of elements with higher oxygen affinity, such as iron, acetone degassing may be required to minimize the oxidation, and that nanoparticle size dependence of the oxidation degree cannot be excluded. Recently, the role of excluding oxygen during PLAL of FeRh in acetone was investigated in detail by systematically excluding the residual water, the dissolved molecular oxygen, and the bound oxygen in the solvent.<sup>90</sup> When argon or an N<sub>2</sub>/H<sub>2</sub> mixture was used as an atmosphere during PLAL in acetone, the detected oxygen was reduced to 9.8 at.% and 6.9 at.%, and an effect of the bound oxygen by replacing acetone with acetonitrile could not be observed. Atom probe tomography revealed 9.6 at.% oxygen in the smaller particles, and no detectable oxygen inside bigger nanoparticle. Hence, according to literature, for PLAL of Cu, acetone

PLAL under sealed conditions may be enough to suppress the oxidation below detection limit, but in general, oxidation cannot be fully excluded even after solvent drying and degassing with reducing gases,<sup>14,89,90</sup> in particular for elements with high oxygen affinity.

Since chemical reactions are not implemented in the simulation, the use of a liquid in the experiments that reduces oxidation can be considered as a good match. Moreover, the mixing between the two components of the bilayer at the initial dynamic stage of laser ablation investigated in the simulations can be expected to have a weak sensitivity to the type of the liquid environment, which mostly provides the conditions for the ablation plume deceleration and cooling of the top part of the plume. The high temperature of the top part of the ablation plume and the lack of direct contact with the liquid environment in the lower part of the plume reduces the likelihood of a substantial effect of the chemical reactions on processes occurring during the first nanoseconds after the laser pulse. Indeed, while the exact time when chemical reactions are setting in during PLAL is yet unknown, the results of recent *in situ* synchrotron X-ray absorption spectroscopy (XAS) measurements performed for PLAL of Zn in water suggest that nanoparticles within the cavitation bubble show a metal signature, without measurable oxidation, even after a hundred of microseconds.<sup>91</sup> These observations indicate that not a significant mass fraction is oxidized during cavitation, even though partial surface oxidation of the nanoparticles could have been below the XAS detection limit.

Overall, the differences in the film thickness, pulse duration, and type of the liquid environment should not prevent us from using the insights into the mechanisms of laser ablation of the bilayer targets obtained in the simulations for interpretation of the experimental observations. The experiments and simulations are performed in the same physical regime, and the conditions in both parts of this study are chosen to provide insights into the key processes defining the composition of nanoparticles produced by PLAL of metal bilayers.

### **3. Results and discussion**

In this section, we report and discuss the results of the computational and experimental investigation of nanoparticle formation in PLAL of Ag-Cu bilayer films. The ablation mechanisms and the processes responsible for the nanoparticle formation are discussed in Sections 3.1 and 3.2 based on the results of two large-scale atomistic simulations performed for Ag on Cu (glass/Cu/Ag) and Cu on Ag (glass/Ag/Cu) bilayer configurations, respectively. The results of the computational analysis of the nanoparticle size distributions, composition of nanoparticles, and correlation between the size and composition are discussed in Section 3.3. The results of the experimental characterization of the ablation spot and nanoparticles are reported in Sections 3.4 and 3.5, respectively.

#### **3.1. Simulation of glass/Cu/Ag bilayer**

The simulation discussed in this section is performed for glass/Cu/Ag bilayer irradiated at an absorbed laser fluence of  $100 \text{ mJ/cm}^2$ , which is significantly above the threshold for an explosive decomposition of the film into vapor and small droplets. A series of snapshots from the simulation shown in Figure 2 provide a clear visual view of the ablation process, where the expanding ablation plume (hot mixture of metal vapor and liquid droplets generated in the phase explosion of the superheated film) is rapidly decelerated by the resistance from the water environment and accumulates at the water-plume interface. The ablation plume deceleration and the formation of a dense hot metal layer at the water-plume interface can also be seen in the density and temperature contour plots shown in Figure 3. The initial rapid expansion of the ablation plume brings the water-plume interface to the level of  $\sim 150 \text{ nm}$  above the substrate during the first  $\sim 300 \text{ ps}$  after the laser pulse and turns into a slower steady upward movement of the interface with a velocity of  $\sim 35 \text{ m/s}$  during the following  $3 \text{ ns}$  of the simulation.

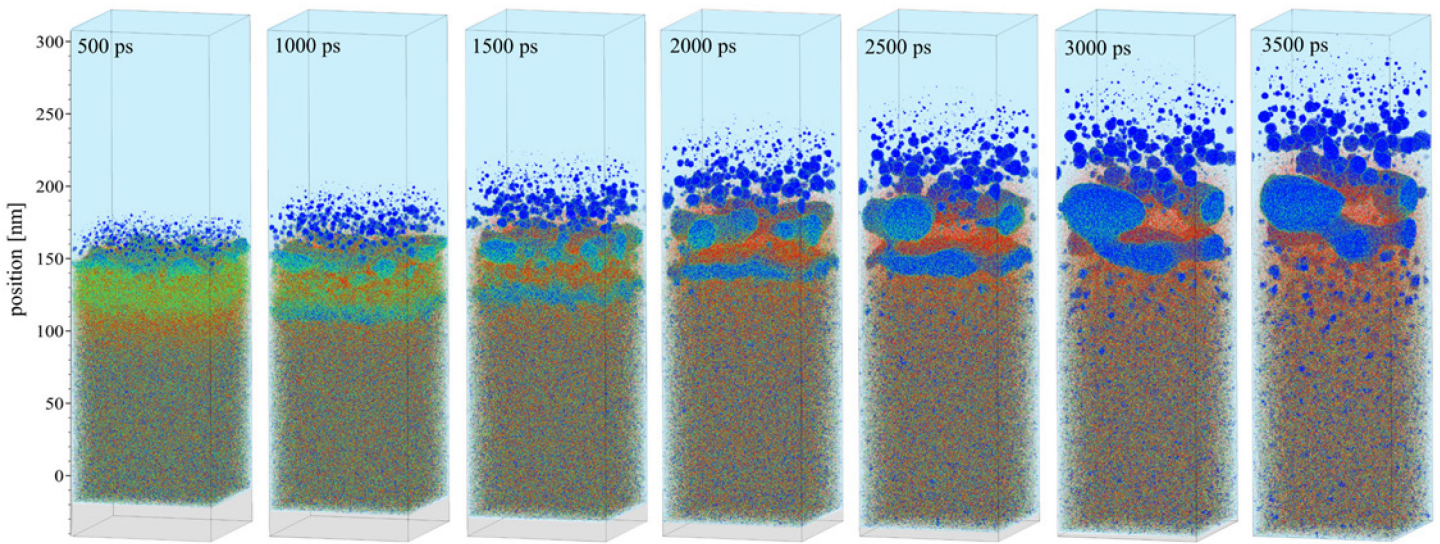


**Figure 2.** Snapshots of atomic configurations obtained in an atomistic simulation of laser ablation of a glass/Cu/Ag bilayer system irradiated in water by a  $100 \text{ fs}$  laser pulse at an absorbed fluence of  $100 \text{ mJ/cm}^2$ . The vertical axis shows the position with respect to the initial location of the silica substrate surface before the irradiation. The transparent silica substrate is represented by the grey rectangular parallelepiped. The atoms are colored by their potential energies, in the range from  $-2$  to  $-1 \text{ eV}$ , so that the blue atoms belong to liquid droplets and the red ones are the vapor-phase atoms. The time after the laser pulse, from  $500 \text{ ps}$  to  $3500 \text{ ps}$ , is marked on the snapshots. The water molecules are not shown to expose the nanoparticle formation, and the presence of water is shown schematically by the blue background. An animated sequence of snapshots from this simulation can be found in the Supporting Information, with atoms colored by potential energy and atom type.

The interfacial metal layer is not uniform but exhibits stratification into three distinct regions, a top region where rapid nucleation and growth of numerous small nanoparticles is observed, a region with a complex coarse morphology of interconnected liquid regions, and an underlying continuous thin metal layer that retains its integrity up to  $\sim 3000 \text{ ps}$ . The stratification can already be seen in the snapshot shown in Figure 2 for  $500 \text{ ps}$ , becomes even more pronounced between  $1000$  and  $2000 \text{ ps}$ , and starts to blur by the end of the simulation, after the onset of decomposition of the bottom metal layer.

The formation of a low-density region at the top of the interfacial layer, which shows up as a blue gradually widening stripe in Figure 3a, is related to the direct interaction of the hot metal plume with the water environment. The water in contact with the hot metal layer is brought to the supercritical state, and the expansion of the supercritical water leads to the formation of a low-density region that serves as a precursor for the formation of a cavitation bubble. The expansion of the supercritical water occurs simultaneously with the active evaporation of hot metal into the low-density region, creating a metal-water mixing region. The conditions in the metal-water mixing region are highly susceptible to the condensation of metal atoms into clusters and the rapid growth of the atomic clusters into nanoparticles.<sup>40,45-47</sup> The temperature in the mixing region, while staying above the critical temperature of water (588 K for the CG model of water),<sup>56</sup> is close to and, in the upper part of the mixing region, even below the melting temperature of Ag (1267 K for the EAM Ag),<sup>60</sup> which is the main component present in this region. As a result, rapid nucleation and growth of the nanoparticles are initiated on a very short timescale of just a few nanoseconds after the laser irradiation, as can be seen from Figure 2. Moreover, the low temperature in the mixing region results in quenching and crystallization of some of the small clusters and droplets in the upper part of this region by the end of the simulation, *i.e.*, only 3.5 ns after the laser pulse.

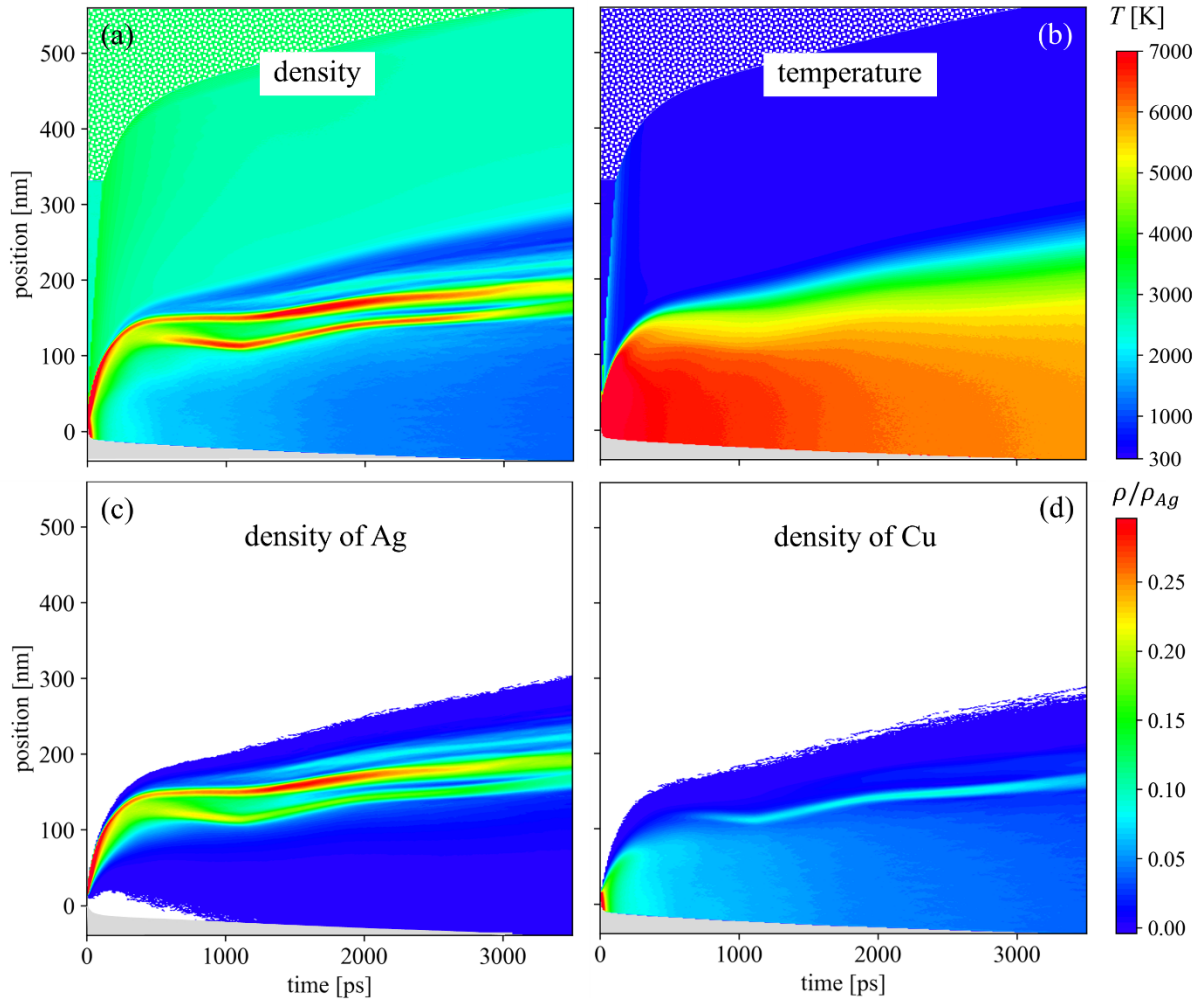


**Figure 3.** Spatial and temporal evolution of density and temperature predicted in the simulation for which snapshots are shown in Figure 2. The total density and the density of silver and copper are shown in (a), (c), and (d), respectively. In all plots, the density is normalized by density of solid silver at 300 K,  $\rho_{Ag}$ , and share the same color scale bar. The grey regions represent the silica substrate. The regions where there are no Ag or Cu atoms are blanked in (c) and (d). The green and blue patterned background in the upper left parts of (a) and (b) represent the implicit presence of water beyond the pressure-transmitting boundary (NRB-W in Figure 1) applied at the top of the water layer explicitly simulated with CG MD.

Below the low-density mixing region, a higher density part of the interfacial layer featuring a coarse morphology of interconnected liquid regions is observed in the snapshots shown in Figure 2. Similarly to earlier studies of laser ablation of thin Ag films<sup>45</sup> and bulk targets,<sup>40,46</sup> the roughening of the interfacial layer and its decomposition into large nanoparticles with diameters on the order of 10 nm can be attributed to the rapid deceleration of the plume and cooling of the metal in direct contact with the water environment. In particular, the deceleration of the higher density metal layer accumulated at the interface by the lighter supercritical water creates classical conditions for the development of Rayleigh-Taylor instability<sup>92</sup> at the water-plume interface. A quantitative analysis reported in Ref. 40, demonstrates that the fastest growing wavelength and the characteristic time of the exponential growth of small perturbations in the Rayleigh–Taylor instability under conditions realized at the initial stage of the plume expansion in PLAL are on the order of tens of nanometers and hundreds of picoseconds, respectively. As a result, by the end of the initial deceleration,  $\sim 300$  ps, the interface develops a rough “terrain” that gradually decomposes into individual liquid droplets, Figure 2.

Overall, the initial dynamics of the ablation process briefly described above for the Ag on Cu bilayer film is similar to that observed in an earlier study of laser ablation of an Ag film in water.<sup>45</sup> There are, however, several notable differences. Firstly, due to the higher laser fluence used in the present study, the complete disintegration of the hot metal layer formed at the interface between the ablation plume and water environment is more prompt and occurs on the timescale of the simulation. As can be seen from Figure 2, the lower part of the dense interfacial region is not directly affected by the rapid roughening at the deceleration stage, but still loses its integrity and undergoes transformation to a large liquid droplet. The formation of the large liquid droplet is affected by the periodic boundary conditions and is discussed in more detail in Section 3.3.

Secondly, the bilayer structure of the film leads to a peculiar pathway of the laser energy redistribution during the time of the electron-phonon equilibration. Even though most of the laser energy is deposited to the electronic subsystem of the top Ag layer, the vibrational/phononic temperature raises faster in the underlying Cu layer, leading to the effective energy redistribution from Ag to Cu. This effect is related to a more than twice stronger electron-phonon coupling in Cu as compared to Ag at room temperature and an even larger difference between the two metals in the electronically excited state.<sup>65</sup> The channeling of the deposited laser energy to the layers with stronger electron-phonon coupling has been predicted in TTM-MD simulations of Au-Cu<sup>93</sup> and Ag-Cu<sup>66</sup> layered systems irradiated in the melting and resolidification regime, observed in time-resolved pump-probe

thermo-reflectivity experiments performed for Au–Cr<sup>94</sup> and Au–Pt<sup>95</sup> layered systems, and found to play an important role in laser nano-structuring of Ag-Cu bilayers.<sup>52</sup> While the small thickness of the individual layers in the present study suppresses the manifestation of this effect, it is still present and is discussed in Section 3.2, where we compare the results of the simulations for glass/Cu/Ag and glass/Ag/Cu bilayers.

Lastly, and most importantly, the bilayer structure of the film makes it possible to investigate the extent of mixing between the two components during the ablation process, as well as the contribution of the two components to the nanoparticles generated in different parts of the emerging cavitation bubble. The implication of the nanoscale separation of the two components in the target bilayer on the composition of nanoparticles generated by PLAL is the main question addressed in the present study. The mixing of the two components in the ablation plume is discussed below, while the results of additional detailed analysis of the nanoparticles are provided in Section 3.3.

The extent of mixing of the two components is illustrated in Figure 4, where the results of a detailed analysis of the final atomic configuration obtained by the end of the simulation are presented. One of the striking observations, apparent from the Ag and Cu number density profiles shown in the left panel of Figure 4, is the direct link between the location of the component in the target and its distribution within the expanding cavitation bubble. The Ag that originates from the top part of the bilayer is almost exclusively located within the dense interfacial region and the low-density water-metal mixing region forming above the interfacial layer. Most of the Cu, on the other hand, is present in the form of vapor phase atoms and small clusters evenly distributed within a wide and expanding space located between the substrate and the interfacial region. From the temperature contour plot shown in Figure 3b we can see that the temperature of the Cu vapor-cluster mixture is only about 15% below the critical temperature of the EAM Cu material,  $T_c = 6350$  K.<sup>62</sup> The expansion of this hot mixture counteracts the pressure exerted on the interfacial region by the supercritical water and keeps pushing the large droplets formed in the interfacial region in the upward direction.

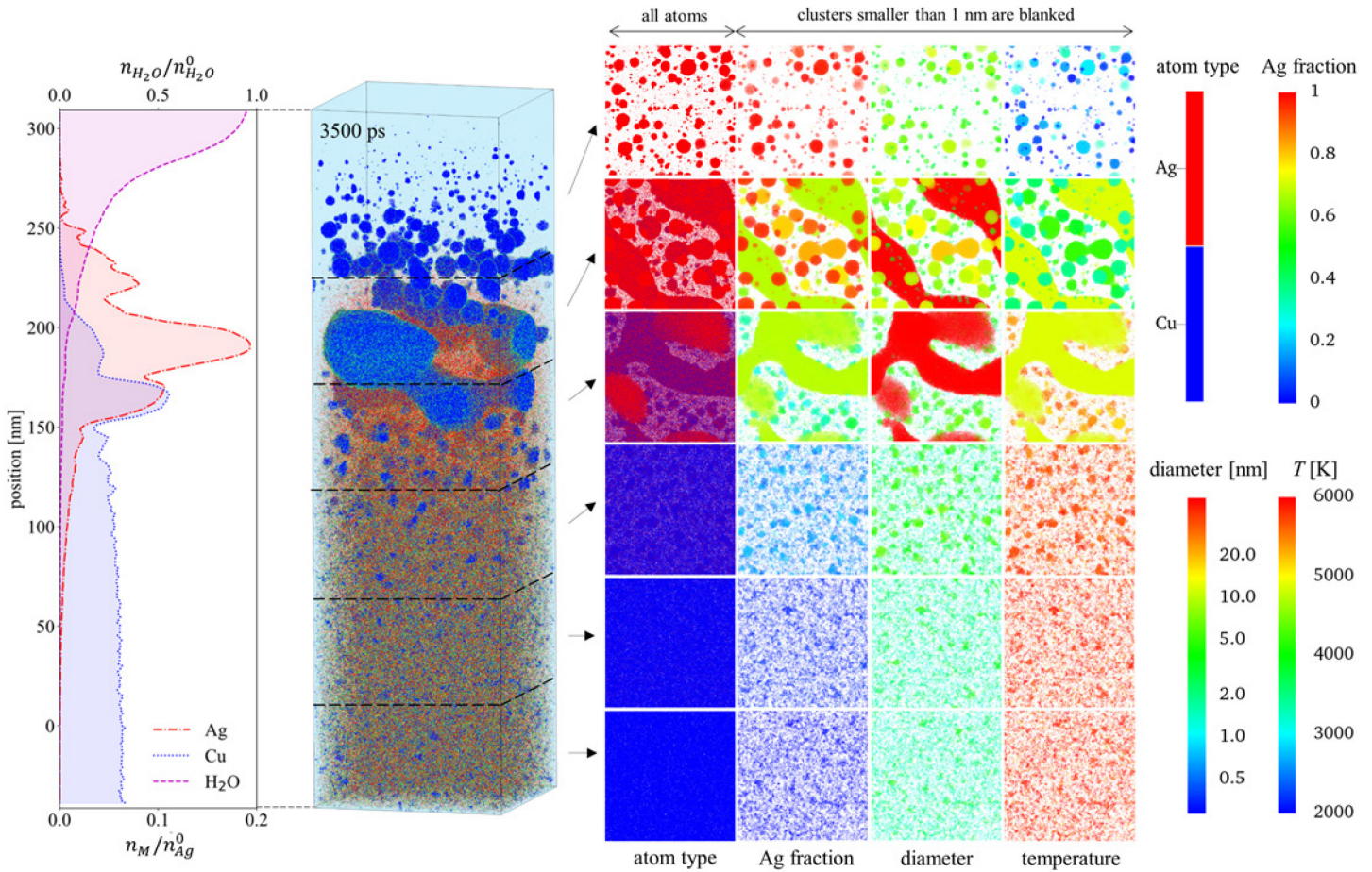


**Figure 4.** Results of detailed analysis of atomic configuration obtained by 3.5 ns in the simulation for which snapshots are shown in Figure 2. The leftmost panel shows the distributions of atomic number densities of Ag (red dash-dotted line), Cu (blue dotted line), and water (purple dashed line) shown for a region from -41 to 309 nm with respect to the initial position of the silica substrate surface before the irradiation. The values of number densities are normalized by the number density of liquid water at 300 K,  $n_{H_2O}^0$ , and solid Ag at 300 K,  $n_{Ag}^0$ , for water and the two metals, respectively. The points where the curves for the two metals cross each other correspond to local equiatomic composition. The next panel shows the atomic snapshot for 3.5 ns aligned with the density plot and colored as described in the caption for Figure 2. The snapshot is split into 6 layers, as shown by dashed lines, and top views of each layer are shown in the four columns located to the right from the snapshot. In the first column, the atoms are colored by atom type, red for Ag and blue for Cu. In the remaining three columns, all individual atoms and clusters smaller than 1 nm in diameter are blanked, and the same color is used for all atoms that belong to the same nanoparticle. The coloring in these columns is by composition (fraction of Ag), size (diameter  $D_e$  of an equivalent spherical particle with the same number of atoms<sup>96</sup>), and average internal temperature  $T$  of the nanoparticles. Note that because of a large variation in the nanoparticle diameters, the logarithmic scale is used for coloring in this case.

The composition of different parts of the expanding ablation plume can also be seen from the top views on different slices of the system shown in the right part of Figure 4. In the first column of the slice, all atoms colored by the atom type (blue for Cu and red for Ag) are shown, while only the nanoparticles with equivalent diameters<sup>96</sup> larger than 1 nm (more than 30 and 44 atoms for pure Ag and Cu nanoparticles, respectively) are shown in the second column. The large liquid droplet of a complex morphology formed in the course of decomposition of the initially continuous metal layer transiently appearing in the lower part of the interfacial

region serves as a demarcation separating the Cu-rich lower and Ag-rich upper parts of the plume. This large liquid droplet itself is predominantly composed of Ag, but has a substantial (32 at.%) presence of Cu.

In general, the limited mixing of the two components separated by only 10 nm from each other in the initial target appears to be surprising given the fact that the whole film undergoes an explosive decomposition into vapor and small droplets at the start of the ablation process. The spatial separation of the two components in the ablation plume (*e.g.*, see the sharp transition from blue to red in the “atom type” column in Figure 4) can be explained, however, by the specifics of the ablation dynamics in a liquid environment discussed at the beginning of this section. The accumulation of the top part of the ablation plume at the interface with the water environment and the formation of a relatively compact transient interfacial layer prevent the rapid vapor-phase mixing and largely preserve the initial layered structure of the target in the ablation plume generated by the end of the initial dynamic stage of the ablation process investigated in the simulation.

### **3.2. *Simulation of glass/Ag/Cu bilayer***

To verify the general character of the computational predictions described in the previous section and to check the dependence of the ablation process on the order in which the two layers are arranged in the bilayer target, in this section we provide a brief discussion of the results of a simulation performed for a glass/Ag/Cu target arrangement. The irradiation conditions in this simulation are the same as those used in the simulation of a glass/Cu/Ag target discussed in the previous section, and the overall picture of the ablation process, as seen from the series of snapshots shown in Figure 5, is also similar. To recap, the whole film undergoes an explosive decomposition into metal vapor, atomic clusters, and small droplets. The expanding ablation plume is decelerated by the water environment, accumulates at the water-plume interface, and forms a hot and dense interfacial metal layer. The dynamic interaction of the hot metal layer with water leads to the splitting of the interfacial layer into two parts by the time of 500 ps. The top part remains in contact with water and decomposes into relatively large (10s of nm) nanoparticles consisting mostly of the component of the top layer. The lower part initially bounces back from water but is then pushed up again by the underlying metal vapor. This layer also decomposes at a longer timescale, between 2 and 3 ns.

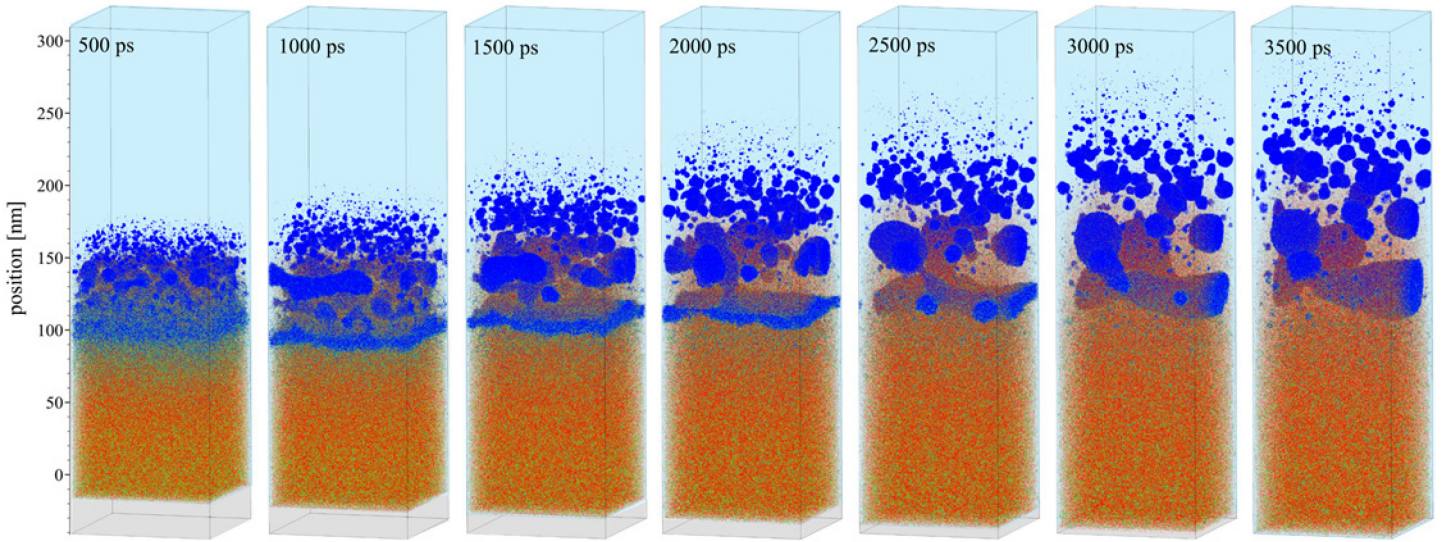


**Figure 5.** Snapshots of atomic configurations obtained in an atomistic simulation of laser ablation of a glass/Ag/Cu bilayer system irradiated in water by a 100 fs laser pulse at an absorbed fluence of  $100 \text{ mJ/cm}^2$ . The vertical axis shows the position with respect to the initial location of the silica substrate surface before the irradiation. The transparent silica substrate is represented by the grey rectangular parallelepiped. The atoms are colored by their potential energies, in the range from -2 to -1 eV, so that the blue atoms belong to the liquid droplets and the red ones are the vapor-phase atoms. The time after the laser pulse, from 500 ps to 3500 ps, is marked on the snapshots. The water molecules are not shown to expose the nanoparticle formation, and the presence of water is shown schematically by the blue background. An animated sequence of snapshots from this simulation can be found in the Supporting Information, with atoms colored by potential energy and atom type.

Despite the similarity of the results obtained in simulations performed for bilayers with different spatial order of Cu and Ag layers, there are some notable differences mainly related to the different strength of electron-phonon coupling in Cu and Ag. As discussed above, in Section 3.1, the stronger electron-phonon coupling in Cu leads to redistribution of the deposited laser energy from Ag to Cu during the time of the electron-phonon equilibration. Since the laser fluence is well above the threshold for the phase explosion, both layers undergo explosive decomposition regardless of the spatial order of the Cu and Ag layers. Nevertheless, the initial energy redistribution still shows up in the temperature contour plot and the evolution of the interfacial layer. In particular, while the temperature of the Cu vapor in the area between the substrate and the interfacial layer remains higher than the temperature of the interfacial layer at all times during the simulation in the glass/Cu/Ag case (Figure 3b), the temperature maximum shifts to the interfacial layer in the case of glass/Ag/Cu (Figure 6b). The higher temperature of the interfacial region has implications on the layer stability against decomposition into droplets. In particular, one can see the appearance of more numerous large (tens of nanometers) droplets in the upper part of the interfacial region in Figures 5 and 7 as compared to Figures 2 and 4. Moreover, the largest liquid droplet appearing in the lower part of the interfacial region is smaller in the case of glass/Ag/Cu as compared to glass/Cu/Ag (see Section 3.3 for a detailed discussion of the droplets).

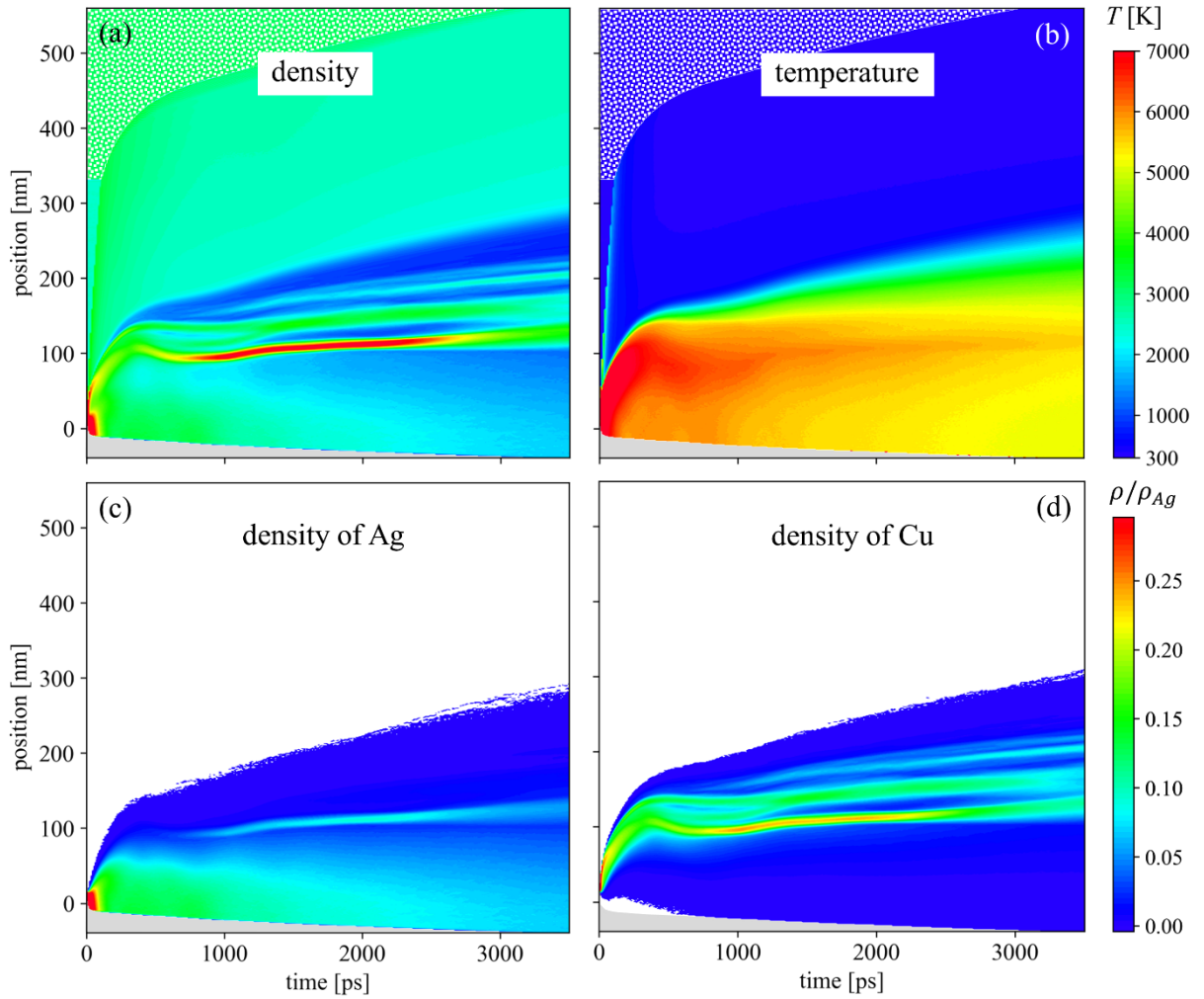


**Figure 6.** Spatial and temporal evolution of density and temperature predicted in the simulation for which snapshots are shown in Figure 5. The total density and the density of silver and copper are shown in (a), (c), and (d), respectively. In all plots, the density is normalized by density of solid silver at 300 K,  $\rho_{Ag}$ , and share the same color scale bar. The grey regions represent the silica substrate. The regions where there are no Ag or Cu atoms are blanked in (c) and (d). The green and blue patterned background in the upper left parts of (a) and (b) represent the implicit presence of water beyond the pressure-transmitting boundary (NRB-W in Figure 1) applied at the top of the water layer explicitly simulated with CG MD.

The number density profiles shown in the left panel of Figure 7 are also reflecting the concentration of energy deposited by the laser pulse in the top Cu layer. The dense interfacial metal layer is wider and located at a lower height above the substrate at the same time of 3.5 ns as compared to the glass/Cu/Ag target, Figure 4, where the energy transfer to the Cu layer creates a stronger upward force exerted by the vaporized Cu on the interfacial layer. The incorporation of Ag into the liquid droplet formed in the lower part of the interfacial region is also reduced in comparison to the Ag-on-Cu simulation, where the lower part of the large liquid droplet has an equiatomic composition. Nevertheless, the most striking observation from the glass/Cu/Ag simulation, the strong spatial segregation of the two bilayer components in the ablation plume, is confirmed in the simulation of the glass/Ag/Cu target. The small clusters forming in the top part of the plume, in the low-density water-metal mixing region consist of almost pure Cu, the larger nanoparticles generated during the decomposition of the interfacial

layer are also predominantly composed of Cu, while the area between the interfacial layer and substrate is filled with vapor, atomic clusters, and small nanoparticles with compositions dominated by Ag.

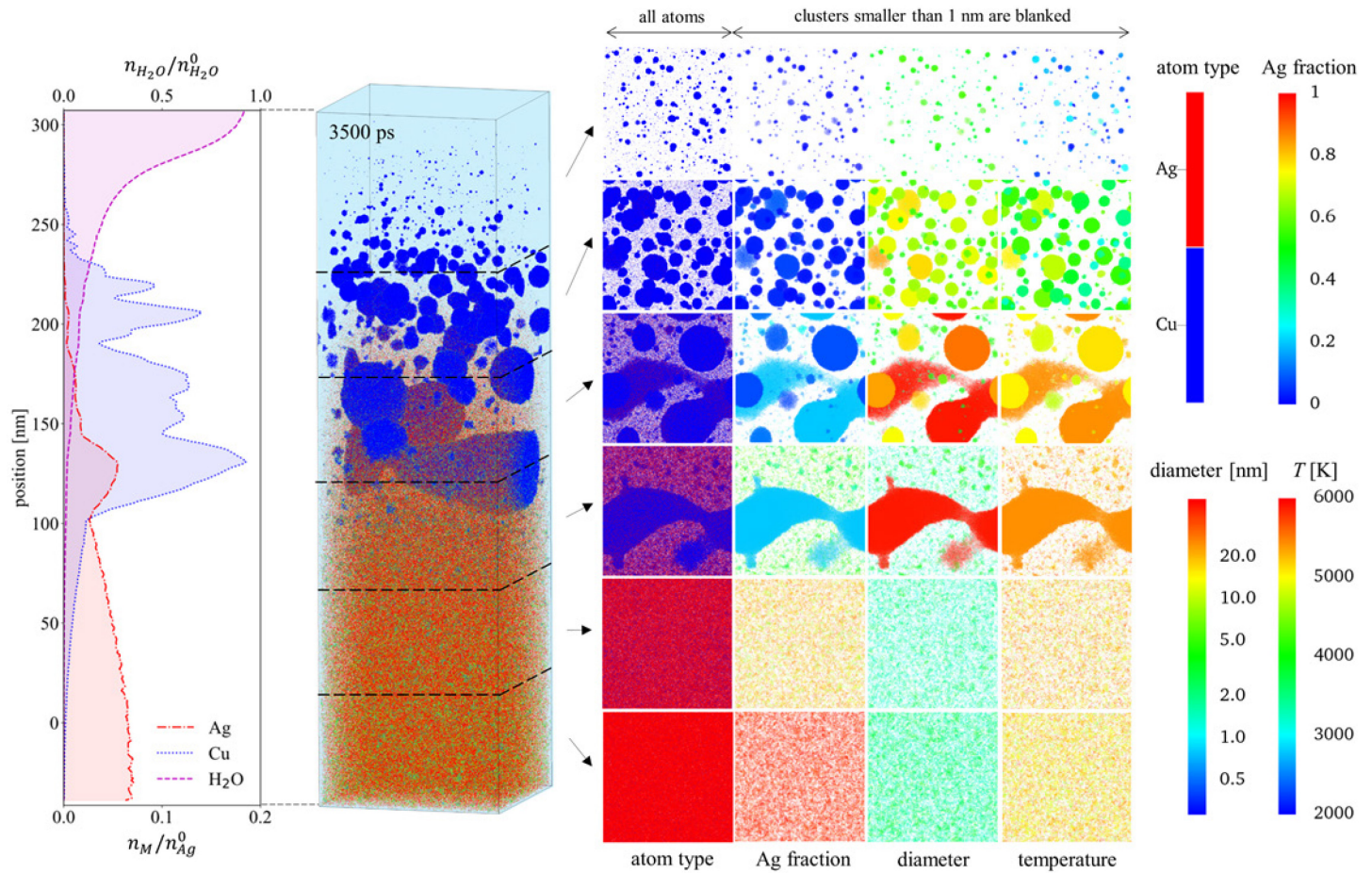


**Figure 7.** Results of detailed analysis of atomic configuration obtained by 3.5 ns in the simulation for which snapshots are shown in Figure 5. The leftmost panel shows the distributions of atomic number densities of Ag (red dash-dotted line), Cu (blue dotted line), and water (purple dashed line) shown for a region from -41 to 307 nm with respect to the initial position of the silica substrate surface before the irradiation. The values of number densities are normalized by the number density of liquid water at 300 K,  $n_{H_2O}^0$ , and solid Ag at 300 K,  $n_{Ag}^0$ , for water and the two metals, respectively. The points where the curves for the two metals cross each other correspond to local equiatomic composition. The next panel shows the atomic snapshot for 3.5 ns aligned with the density plot and colored as described in the caption for Figure 5. The snapshot is split into 6 layers, as shown by dashed lines, and top views of each layer are shown in the four columns located to the right from the snapshot. In the first column, the atoms are colored by atom type, red for Ag and blue for Cu. In the remaining three columns, all individual atoms and clusters smaller than 1 nm in diameter are blanked, and the same color is used for all atoms that belong to the same nanoparticle. The coloring in these columns is by composition (fraction of Ag), size (diameter  $D_e$  of an equivalent spherical particle with the same number of atoms<sup>96</sup>), and average internal temperature  $T$  of the nanoparticles. Note that because of a large variation in the nanoparticle diameters, the logarithmic scale is used for coloring in this case.

### 3.3. Computational predictions on nanoparticle composition and size distribution

In this section, we report the results of a detailed analysis of nanoparticles present in different parts of the simulated system at a time of 3.5 ns after the laser pulse. When comparing the results of this analysis with

experimental observations reported in Section 3.5, we should keep in mind that the nanoparticle composition and size distributions are very likely to undergo substantial changes in the course of further expansion and collapse of the cavitation bubble occurring on the timescale of tens and hundreds of microseconds. The computational prediction that a large number of nanoparticles are already formed during the first nanoseconds of the ablation process, however, makes it reasonable to expect that some of the characteristics of the “early” nanoparticles are retained in the “final” colloidal nanoparticles produced by PLAL. Indeed, the fraction of atoms that belong to the nanoparticles with effective diameters larger than 1 nm is already 68% for the glass/Cu/Ag bilayer system and 76% for the glass/Ag/Cu system at 3.5 ns (see Table 1), suggesting that further longer-term processes of condensation, evaporation, and coalescence are unlikely to “erase” the general trends predicted in the simulations.

**Table 1.** The total number of atoms in the bilayer systems and the number of atoms in the vapor phase (monomers), atomic clusters with effective diameters less than 1 nm, and nanoparticles with effective diameters larger than 1 nm identified at 3.5 ns after the laser pulse in the two simulations discussed in Sections 3.1-3.3.

	<b>Total number of atoms</b>	<b>Number of vapor-phase atoms</b>	<b>Number of atomic clusters (<math>D_e \leq 1</math> nm)</b>	<b>Number of nanoparticles (<math>D_e &gt; 1</math> nm)</b>
<b>glass/Cu/Ag</b>	14,046,208	694,446 (5%)	3,804,810 (27%)	9,546,952 (68%)
	5,760,000 Ag	170,367 Ag + 524,079 Cu	503,288 Ag + 3,301,522 Cu	5,086,345 Ag + 4,460,607 Cu
<b>glass/Ag/Cu</b>	8,286,208 Cu	633,966 (4%)	2,801,407 (20%)	10,610,835 (76%)
		476,051 Ag + 157,915 Cu	2,056,152 Ag + 745,255 Cu	3,227,797 Ag + 7,383,038 Cu

We start the analysis with the largest liquid droplets formed in the two simulations through the decomposition of the transient continuous layer generated in the lower part of the interfacial region. The snapshots of the two droplets are shown in Figure 8, where the Ag and Cu atoms are colored red and blue, respectively. The shapes of these large droplets continue to evolve, and this evolution is affected by the periodic boundary conditions applied in the lateral (horizontal) directions. Indeed, the droplets extend through the whole computational cell, leading to the formation of a continuous liquid structure in one or both horizontal directions. While this effective self-interaction of the large liquid droplets through the opposite sides of the computational cell is an artifact of the finite size of the systems used in the simulations, this artificial effect itself is notable, as it reflects the unexpectedly large size of the droplets. Converting the number of atoms in the large droplets to the equivalent diameter of spherical droplets,<sup>96</sup> we get the diameters of 52 and 46 nm for the glass/Cu/Ag and glass/Ag/Cu bilayers, respectively, which are more than twice larger than the thickness of the original bilayer films. This computational prediction contradicts the conventional picture of nanoparticle formation through a gradual growth from products of explosive disintegration of an irradiated film into a mixture of vapor, atomic

clusters, and small droplets, but is consistent with experimental observations of nanoparticles with maximum sizes significantly exceeding the thickness of the target bilayers discussed in Section 3.5.

The simulations provide a plausible explanation of the formation of large nanoparticles, suggesting that these nanoparticles do not form directly in the course of the explosive disintegration of the thin film targets, but are generated through a multistep process involving the ablation plume accumulation at the interface with the liquid environment, the generation of a hot and relatively dense interfacial metal layer, and the subsequent decomposition of this interfacial layer into large liquid droplets. The maximum size of the droplets is defined by the relatively slow dynamics of the interfacial layer disintegration, which may involve pulling of the hot molten metal distributed over a large spatial extent within the interfacial layer into a single droplet. According to this mechanism, the ablation of a thicker target film ( $\sim 80$  nm in experiment vs. 20 nm in simulations) would produce a thicker and more stable interfacial layer, which would yield larger droplets upon the interfacial layer decomposition. Indeed, the nanoparticles with diameters in the range of hundreds of nanometers have been observed in the experiments discussed in Sections 3.4 and 3.5.

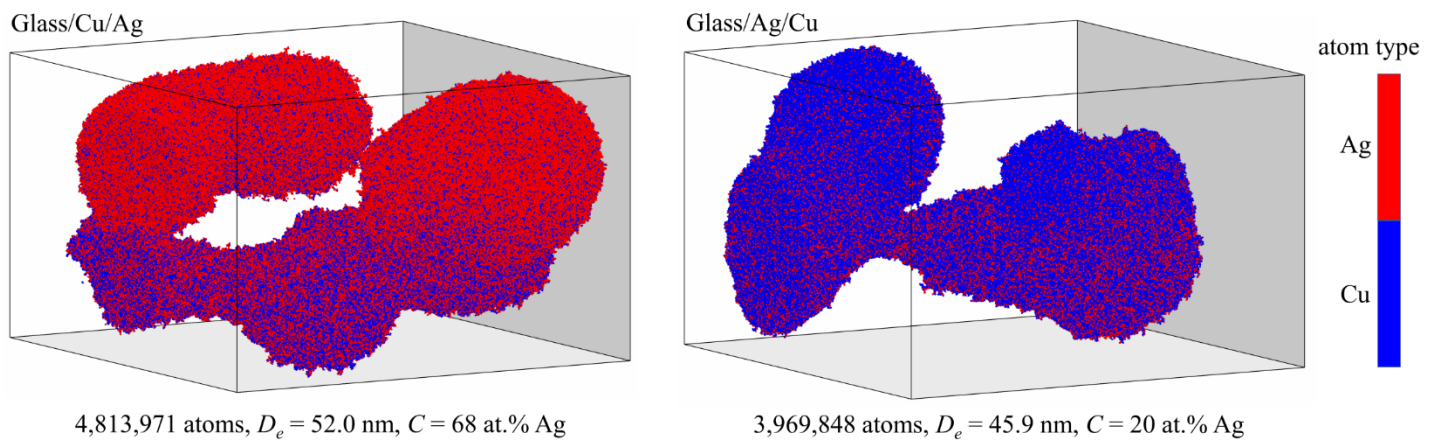


**Figure 8.** Atomic configurations of the largest droplets identified in the simulations illustrated in Figures 2 and 5 at 3.5 ns after the laser pulse. The black boxes show the boundaries of the computational cell in the lateral (horizontal) directions, with periodic boundary conditions applied in these directions.

Turning to the analysis of the composition of the two largest droplets, the dominant colors of the two images shown in Figure 8 clearly indicates that the droplets are mostly composed of the components originating from the top layers of the bilayer targets, with 68 at.% Ag for the glass/Cu/Ag bilayer and 80 at.% Cu for the glass/Ag/Cu bilayer. The minority components in the droplets are distributed unevenly and are concentrated in the lower parts of the droplets. Given the high temperature of the droplets and the long time it would take for them to cool down to below the melting temperature and solidify, however, one can expect that the composition will become spatially homogeneous in the molten droplets, before the phase separation into Ag-rich and Cu-rich regions could take place during the solidification of this eutectic system.

The formation of the continuous interfacial layer gradually decomposing into large droplets creates a barrier hampering the expansion of the underlying hot mixture of vapor, atomic clusters, and small nanoparticles originating from the bottom layer of the bilayer film. This effect can be clearly seen from Figure 9a, where each nanoparticle with  $D_e > 1$  nm is represented by a dot, and the red and blue shadow stripes mark the location of the lowest part of the large droplets generated from decomposition of the interfacial layer in the two simulations. In both cases, the dots tend to concentrate to the left from the stripes, reflecting the presence of a barrier for the free expansion of the plume. This barrier also prevents rapid vapor-phase mixing of the two components at the initial stage of the ablation process and is responsible, to a large extent, for the sharp differences in the composition of nanoparticles generated in different parts of the emerging cavitation bubble. This can be clearly seen from Figure 9a, where the ordinate shows the nanoparticle composition in at.% of the top metal component. Indeed, although the composition is nearly equiatomic in the immediate vicinity of the red and blue stripes, the nanoparticles formed at the front of the bubble, in the water-plume mixing region, consist almost exclusively of the top layer components, whereas the nanoparticles closest to the substrate have compositions of almost pure components of the lower layers.

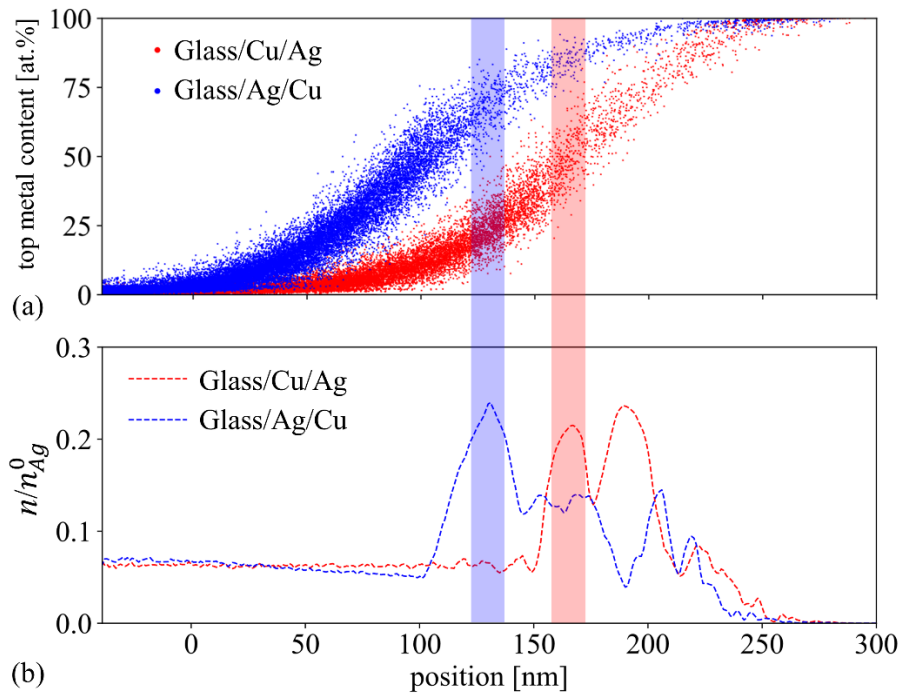


**Figure 9.** Composition of nanoparticles with effective diameter  $D_e$  larger than 1 nm (a) and the total metal number density distributions (b) as functions of the distance from the initial position of the silica substrate surface. The data is plotted for a time of 3.5 ns after the laser pulse for the two simulations of metal bilayers illustrated by snapshots in Figures 2 and 5. In (a), the red and blue dots show the Ag and Cu content of individual nanoparticles generated in simulations performed for bilayers with Ag and Cu as top layers, respectively. In (b), the red and blue dashed lines show the combined number density of both silver and copper atoms predicted in the two simulations. The red and blue shadow stripes mark the first high-density peaks that correspond to the regions where the large droplets are present in the two simulations. The presence of the large droplets hampers the expansion of the underlying region where a hot mixture of vapor, atomic clusters, and small nanoparticles, mostly consisting of the lower layer component, is present.

The nanoparticles formed in the region between the substrate and the interfacial layer are much more numerous as compared to the ones formed in the water-plume mixing region. As a result, these nanoparticles dominate the size distribution shown in Figure 10a, where each bar corresponds to the fraction of nanoparticles that fall within the corresponding bin of nanoparticle diameters. In the range of diameters shown in the distribution,  $1 \text{ nm} < D_e < 4 \text{ nm}$ , most of the nanoparticles are located in this lower region, below the interfacial layer, with only a minor contribution coming from small nanoparticles generated in the top part of the system, in the water-plume mixing region. The larger nanoparticles, exceeding 4 nm, are less numerous but are making a substantial contribution to the distributions weighted by the number of atoms constituting the nanoparticles shown in Figure 10b. Most of these nanoparticles are generated in the process of decomposition of the interfacial region, as can be seen from the series of snapshots of atomic configurations shown in Figures 2 and 5, as well as from the top views of slices of the computational systems colored by the nanoparticle diameters shown in Figures 4 and 7. The largest droplets shown in Figure 8 alone contain 34% and 28% of the total number of atoms in the simulations performed for Ag on Cu and Cu on Ag bilayers, respectively. The contribution of these largest droplets to the probability density functions shown in Figure 10b is reflected by the rightmost wide bars in the plots.

The formation of nanoparticles of different sizes in different parts of the expanding cavitation bubble has direct implications for the distribution of the nanoparticles by composition shown in Figure 11. The composition of the largest fraction of nanoparticles is dominated by the component coming from the lower layer of the bilayer film, Figure 11a. These are the small but numerous nanoparticles formed in the lower and central parts of the system, between the substrate and the interfacial region. The closer a nanoparticle is to the substrate, the lower the concentration of the top layer component in the nanoparticle tends to be, as can be seen from the upper panel of Figure 9. The larger nanoparticles generated within the interfacial region are contributing to relatively low but noticeable tails of the distributions shown in Figure 11a, which extend towards the compositions that correspond to the top layers. The bumps at the end of these tails correspond to the population of smaller nanoparticles formed through the nucleation and growth in the water-plume mixing regions. The distributions weighted by the number of atoms in the nanoparticles of different sizes, shown in Figure 11b, provide an additional evidence of the lack of mixing between the two components of the bilayer targets prior to the formation of the nanoparticles. For both bilayer targets, broad minima are observed in the central parts of the distributions, which correspond to well-mixed compositions of the nanoparticles, while most of the material comprising the nanoparticles tend to have composition dominated by one of the components.

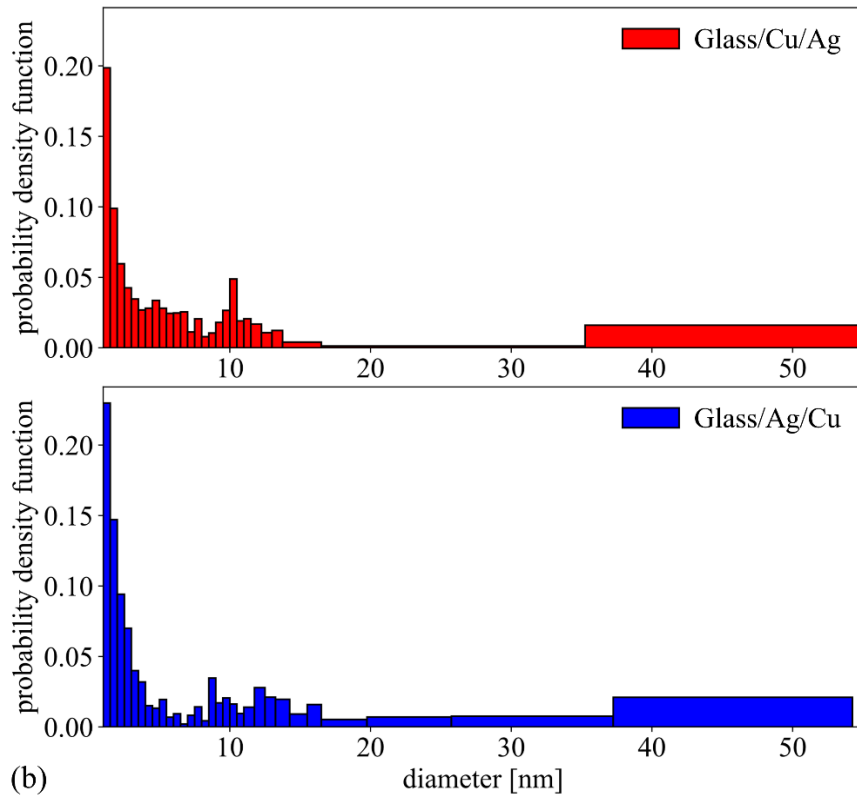
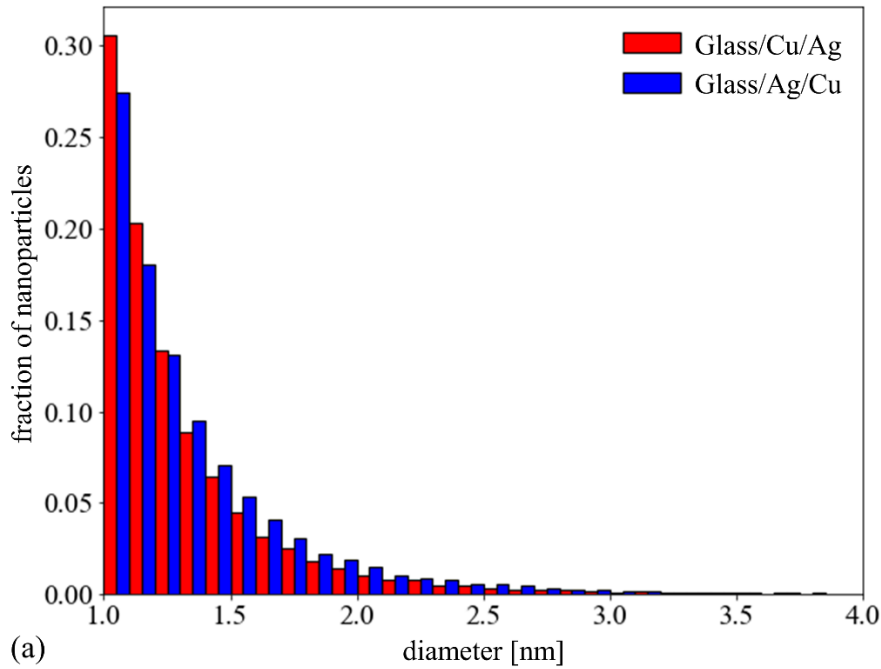


**Figure 10.** Nanoparticle size distributions calculated for final configurations predicted for 3.5 ns after the laser pulse in two simulations of laser ablation of glass/Cu/Ag (red) and glass/Ag/Cu (blue) bilayer films. The distributions are shown for nanoparticles with  $D_e > 1$  nm in the form of fractions of nanoparticles counted within 0.1 nm-wide ranges of corresponding effective diameters (a) and as probability density functions based on the number of atoms in nanoparticles of different sizes (b). In (a), the height of a bar shows the probability that a randomly chosen nanoparticle falls within a particular size range defined by the location and width of the corresponding bin. In (b), the area of each bar corresponds to the probability that an atom randomly picked from any of the nanoparticles with  $D_e > 1$  nm will belong to a nanoparticle that falls within the corresponding size range. Because of the small number of the large droplets in the simulation domain, the width of the bins in (b) is increased so that each bin has at least one droplet.

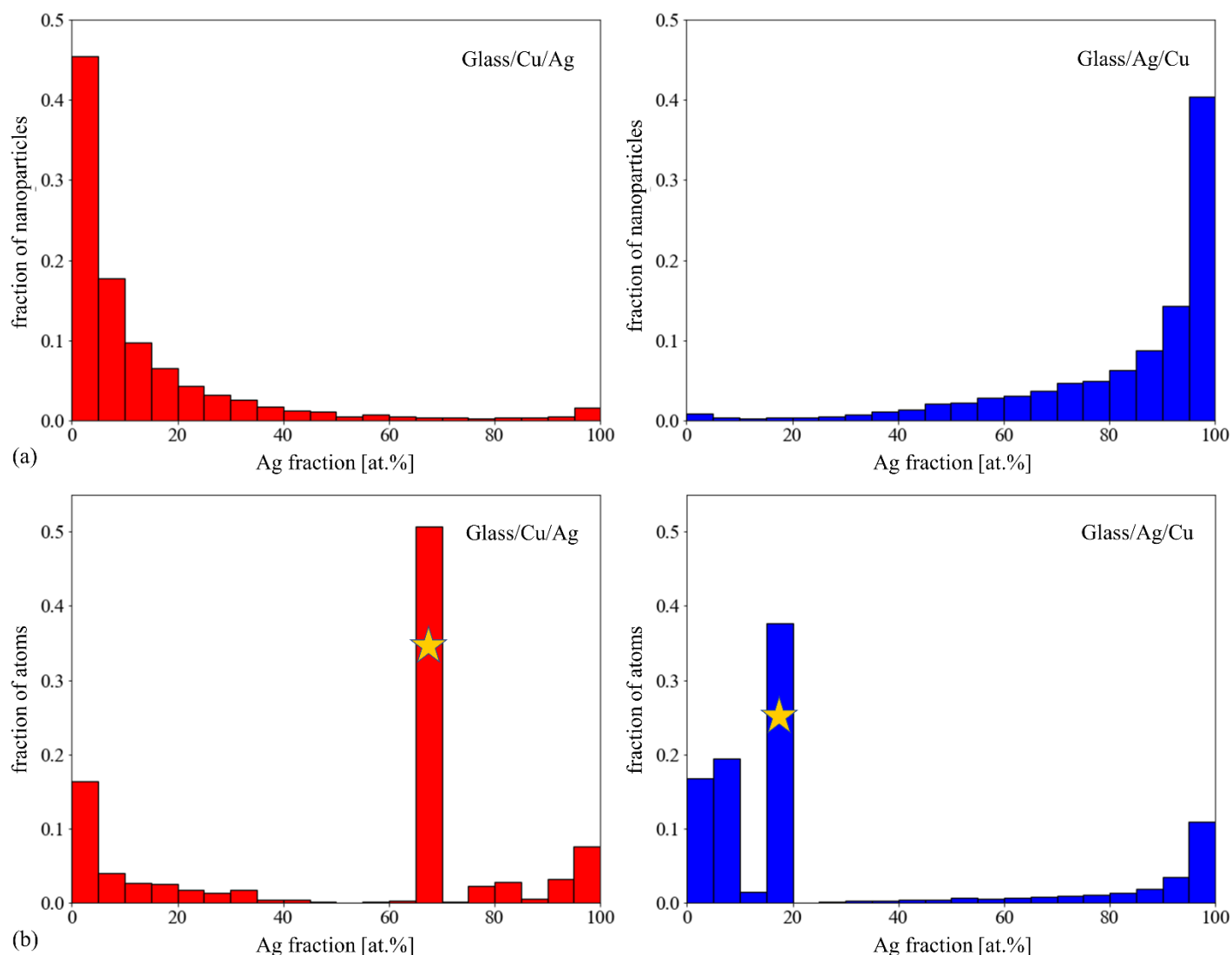


**Figure 11.** The distribution of compositions of nanoparticles with  $D_e > 1$  nm generated in simulations of laser ablation of glass/Cu/Ag (red bars) and glass/Ag/Cu (blue bars) bilayers in water. In (a), the height of each bin shows the fraction of nanoparticles that are within a 5 at.-%-wide range of the corresponding composition. In (b), the height of each bin shows the fraction of atoms in nanoparticles that fall within the corresponding range of compositions. The two bars that include contributions from the two largest droplets shown in Figure 8 are marked by yellow stars.

The correlation between the nanoparticle size and composition can be seen more clearly in the distribution of nanoparticles by diameter and composition shown in Figure 12, where the color of dots reflects the number of nanoparticles with the corresponding size and composition. The highest concentration of nanoparticles is observed at small sizes and compositions dominated by the component from the lower layer of the bilayer systems, *i.e.*, Cu in the case of Ag on Cu bilayer and Ag in the case of Cu on Ag bilayer. This observation is consistent with the distributions shown in Figure 11a. On the other sides of the composition range, we see both the small spikes of the number of small nanoparticles originating from the water-plume mixing region and the presence of large nanoparticles generated through decomposition of the interfacial region. Although the distributions shown in the two panels of Figure 12 look almost as mirror images of each other, a closer look reveals notable differences

related to the channeling of the deposited laser energy to the Cu layer discussed above, in Sections 3.1 and 3.2. The differences include an appearance of a group of mid-size (4-8 nm) nanoparticles with composition dominated by the lower layer component in the case of glass/Cu/Ag target (upper panel of Figure 12), as well as an enhanced population of large (> 12 nm) nanoparticles composed of the top layer component in the case of glass/Ag/Cu target (lower panel of Figure 12). Overall, however, regardless of the order of the layers, the results of the simulations predict the limited mixing of the two components of thin bilayer films ablated in a liquid environment and suggest an explanation of this surprising observation based on the specific mechanisms of ultrashort pulse laser ablation in liquids. The experimental verification of the computational predictions is reported below.

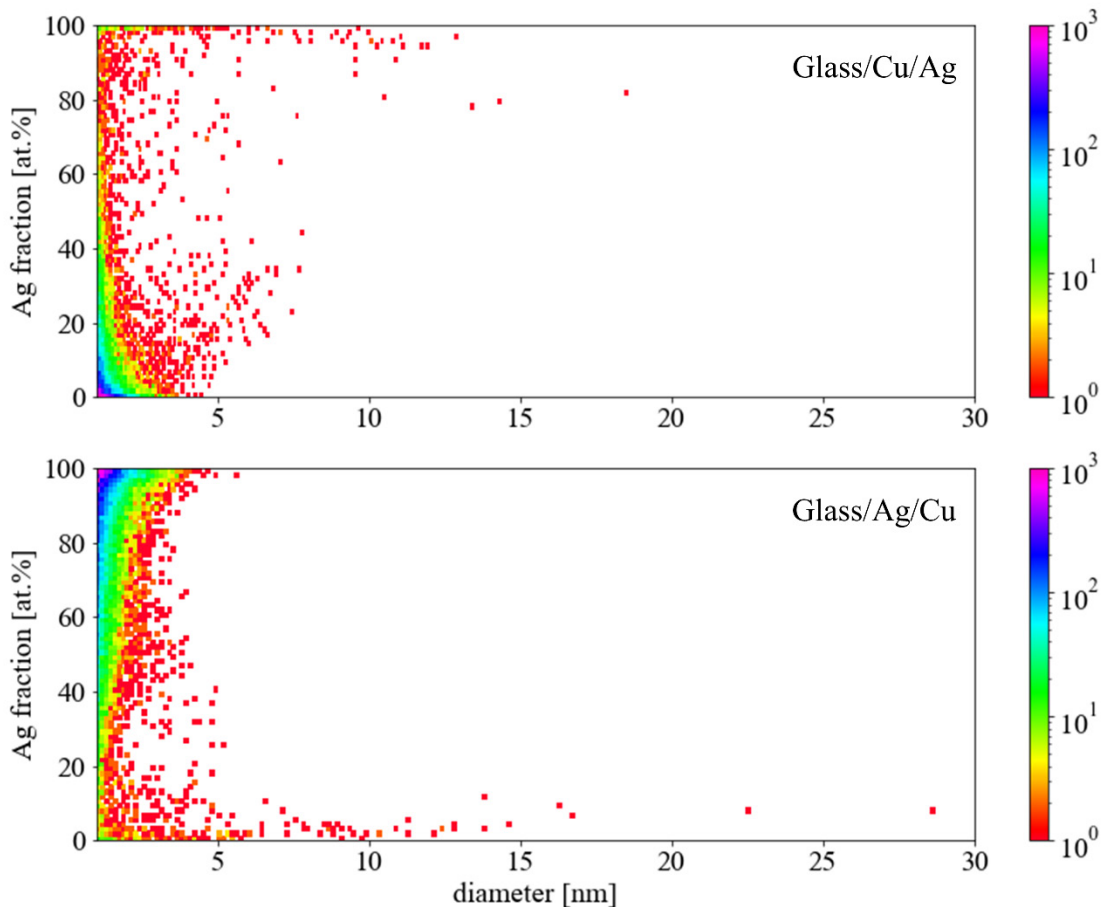


**Figure 12.** The distribution of nanoparticles by diameter and composition predicted in simulations of laser ablation of glass/Cu/Ag (upper panel) and glass/Ag/Cu (lower panel) bilayers in water. The results are shown for a time of 3.5 ns after the laser pulse. The points are colored according to the number of nanoparticles in each of the 0.1 nm-wide and 1.0 at.-%-tall bins covering the parameter space. The red color corresponds to only one nanoparticle in a bin. The largest droplets generated in the simulations ( $D = 52$  nm, 68 at.% Ag in the silver top bilayer and  $D = 46$  nm, 20 at.% Ag in the copper top bilayer) are not shown in the plots.

### 3.4. Experimental results: Characterization of the target film and ablation spot

In order to properly correlate the simulation data with the experimental finding, the thin film targets used in the ablation experiments were analyzed. The results of the analysis of the target films by SEM and EDX are shown in Figure 13 for both glass/Ag/Cu and glass/Cu/Ag film targets. In Figure 13a, the high magnification

SEM images illustrate the two-layer system with Ag appearing slightly brighter than Cu, while the glass substrate is dark grey. Since tilted SEM image may under- or overestimate the thickness, we extract information of the individual layer thickness from EDX point measurements considering the layer stacking (see methods). Figure 13b shows two exemplary EDX spectra for the glass/Ag/Cu and glass/Cu/Ag film targets. The upper layer damps the X-ray lines of the lower layer. We evaluate total thicknesses of 88 nm (65 nm Cu, 23 nm Ag) and 79 nm (39 nm Ag, 40 nm Cu) for glass/Ag/Cu and glass/Cu/Ag targets, respectively. This corresponds to nominal atomic compositions (Cu/Ag) of 80.4/19.6 mol% and 59.2/40.8 mol% for the glass/Ag/Cu and glass/Cu/Ag bilayers, respectively.

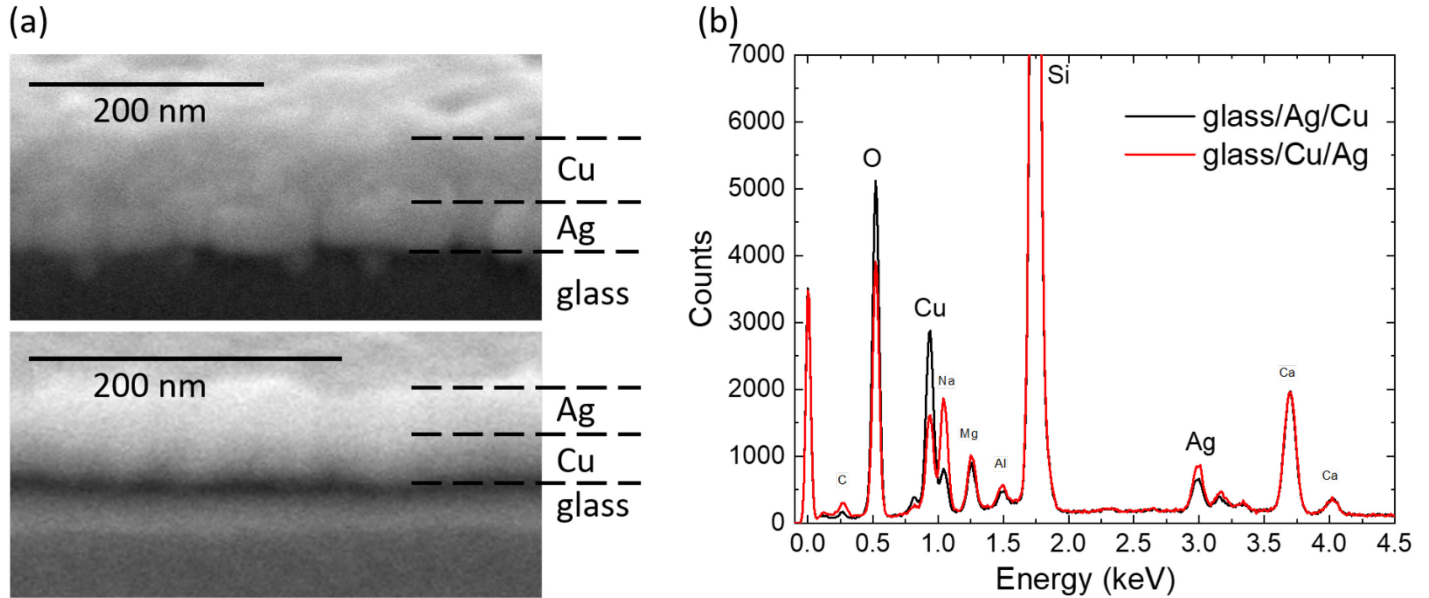


**Figure 13.** Left: SEM images of a cut section of a glass/Ag/Cu and glass/Cu/Ag systems, illustrating the metal layers (light grey) on top of the glass substrate (dark grey). Right: EDX spectra from both samples showing the main elements of glass (Si, O) and metal layers (Cu and Ag). Na, Mg, Al, and Ca are additional elements in the glass substrate. It is apparent that the layer sequence determines the intensity of Ag and Cu X-ray lines.

Consecutively, we analyzed the thin film targets after single-pulse laser ablation in acetone via SEM and measured the elemental composition of the ablation spot by EDX line scans (Figure 14). The analysis of the ablation spot clearly indicates the presence of particles in the size range from 2  $\mu\text{m}$  down to nanoparticles. These particles predominantly have a spherical geometry and are broadly distributed throughout the spot, with the larger particles concentrated in the periphery of the ablation spot. The presence of these particles can be attributed to the spatial variation of processes induced by the laser beam characterized by a Gaussian energy distribution. In the central part of the laser spot, the energy density deposited by the laser pulse is sufficient to bring the film material to the state of the strong superheating, leading to the explosive phase decomposition into vapor and small droplets, as observed in the simulations described in Sections 3.1-3.3. In the periphery, however, the reduced energy density may only be sufficient for melting and/or spallation of the film. The molten film separated/spalled from the substrate can undergo disintegration into large droplets,<sup>97,98</sup> whereas the molten film that remains on the substrate

can decompose into droplets through the dewetting process.<sup>99-101</sup> The lateral pressure gradients and active motion in the liquid environment caused by the ablation of the central part of the irradiated spot can facilitate the film decomposition and can also spread the large droplets and pieces of debris within and even outside the ablated spot, as can be seen from SEM images shown in Figure 14. Some of the smaller nanoparticles observed in these images may also originate from redeposition of nanoparticles generated by laser ablation.

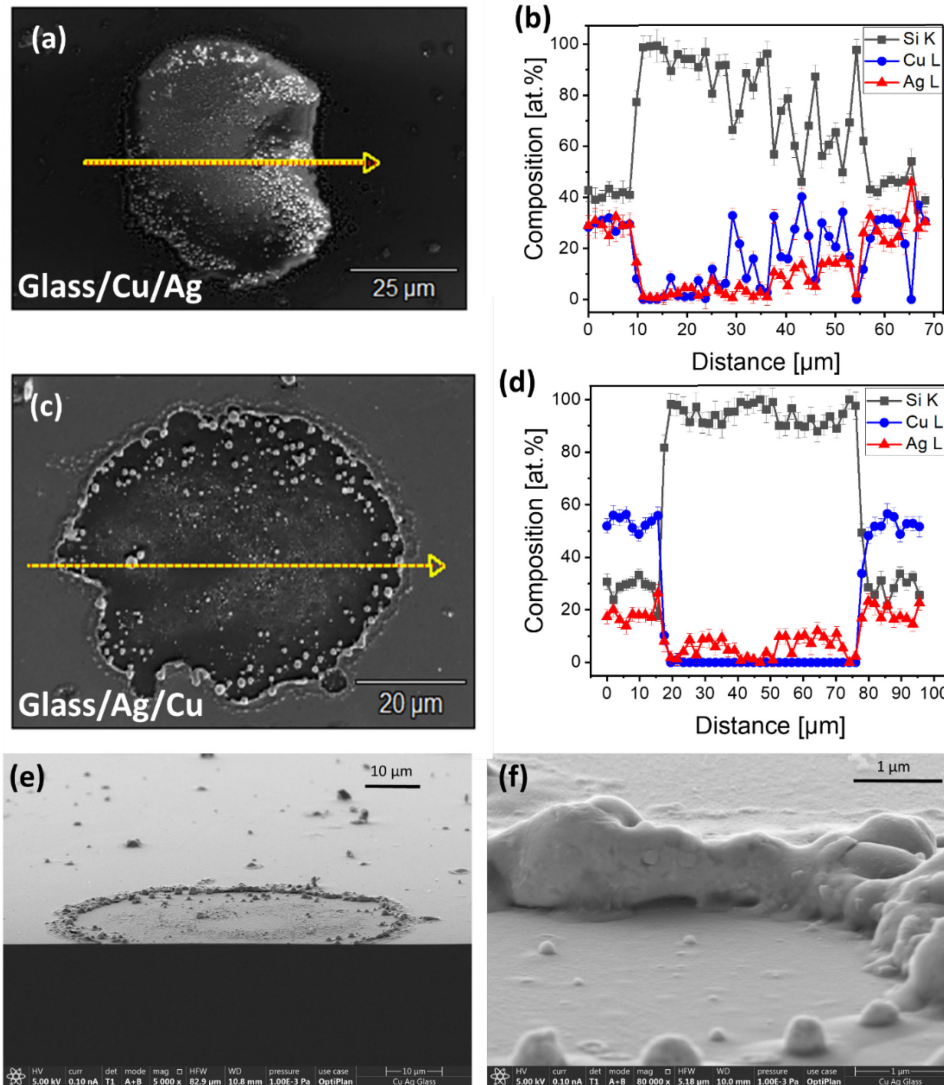


**Figure 14.** (a) Top-view SEM image of an ablation spot on a glass/Cu/Ag target, with the yellow arrow indicating the course of an EDX line scan. (b) EDX line scan of an ablation spot on a glass/Cu/Ag target. (c) Top-view SEM image of an ablation spot on a glass/Ag/Cu thin film target, with the yellow arrow indicating the course of an EDX line scan. (d) EDX line scan of an ablation spot on a glass/Ag/Cu target. (e), (f) SEM images of an exemplary ablation spot on a glass/Ag/Cu target.

The results of EDX measurements shown in Figure 14b,d demonstrate that the area of the ablation spot is dominated by the Si signal, which is a clear indication that the majority of the metal thin film has been ablated. Nonetheless, the EDX line scans show that the debris particles within the ablation spot are exclusively made of silver in the glass/Ag/Cu case and show an excess of copper in the glass/Cu/Ag case. It is likely that the presence

of metal within the ablation spot is related to redeposition of the ablation plume, potentially during the cavitation bubble oscillation. The dominant presence of the lower layer component in the redeposited material is consistent with the results of the simulations, which show that the lower part of the ablation plume is mostly composed of material originating from the lower layer of the bilayer film, *e.g.*, see Figure 9a. Although the results of the simulations are shown for the initial stage of the ablation process while the redeposition is expected to occur on a much later time, the prompt conversion of the top layer material into the nanoparticles produced through the interfacial layer decomposition, *e.g.*, see Figures 4 and 7, suggests that the lower part of the plume is likely to remain depleted of the top layer component even at much longer timescales and underlines our hypothesis of strong elemental segregation during PLAL.

### 3.5. *Experimental results: Characterization of nanoparticles*

In this section, we characterize the compositions and size distributions of nanoparticles produced in picosecond laser ablation experiments and compared their properties to those predicted in the simulations for the initial stage of the ablation process described in Sections 3.1-3.3. We aim to elucidate to what extent the computational predictions on early-stage particle formation are in accordance with experimental results, representing the endpoint of the particle formation process. As detailed in Section 2.2, the experiments are performed for glass/Cu/Ag and glass/Ag/Cu films with an overall thickness of about 80 nm (see Section 3.4), and the ablation is conducted in acetone to minimize oxidation. The nanoparticle size distributions are obtained through analysis of TEM images, and the compositions at a single particle level are evaluated by EDX for 40-50 particles per sample. The overall composition was not determined by TEM-EDX, as the density of nanoparticles on the TEM grids was too low.

The number-weighted nanoparticle size distributions (Figure 15) clearly show the presence of nanoparticles with a broad range of diameters dominated by nanoparticles with diameters below 20 nm. Median nanoparticle diameters, derived from log-normal fits, are 8 and 10 nm for glass/Cu/Ag and glass/Ag/Cu targets, respectively. Furthermore, several individual nanoparticles with diameters exceeding 100 nm are observed, with the largest particles formed from the glass/Cu/Ag target arrangement. These experimentally determined nanoparticle size distributions are in good agreement with those predicted in the simulations (Figure 10). The diameters of the largest nanoparticles found in the analysis of the experimental TEM images, however, are significantly larger than those generated at the initial stage of the ablation process investigated in the simulations. The largest spherical nanoparticles identified in experiments performed for glass/Ag/Cu and glass/Cu/Ag bilayers have diameters up to about 150 and 900 nm, respectively, while the largest liquid structures observed in the simulations have a diameter of about 50 nm.

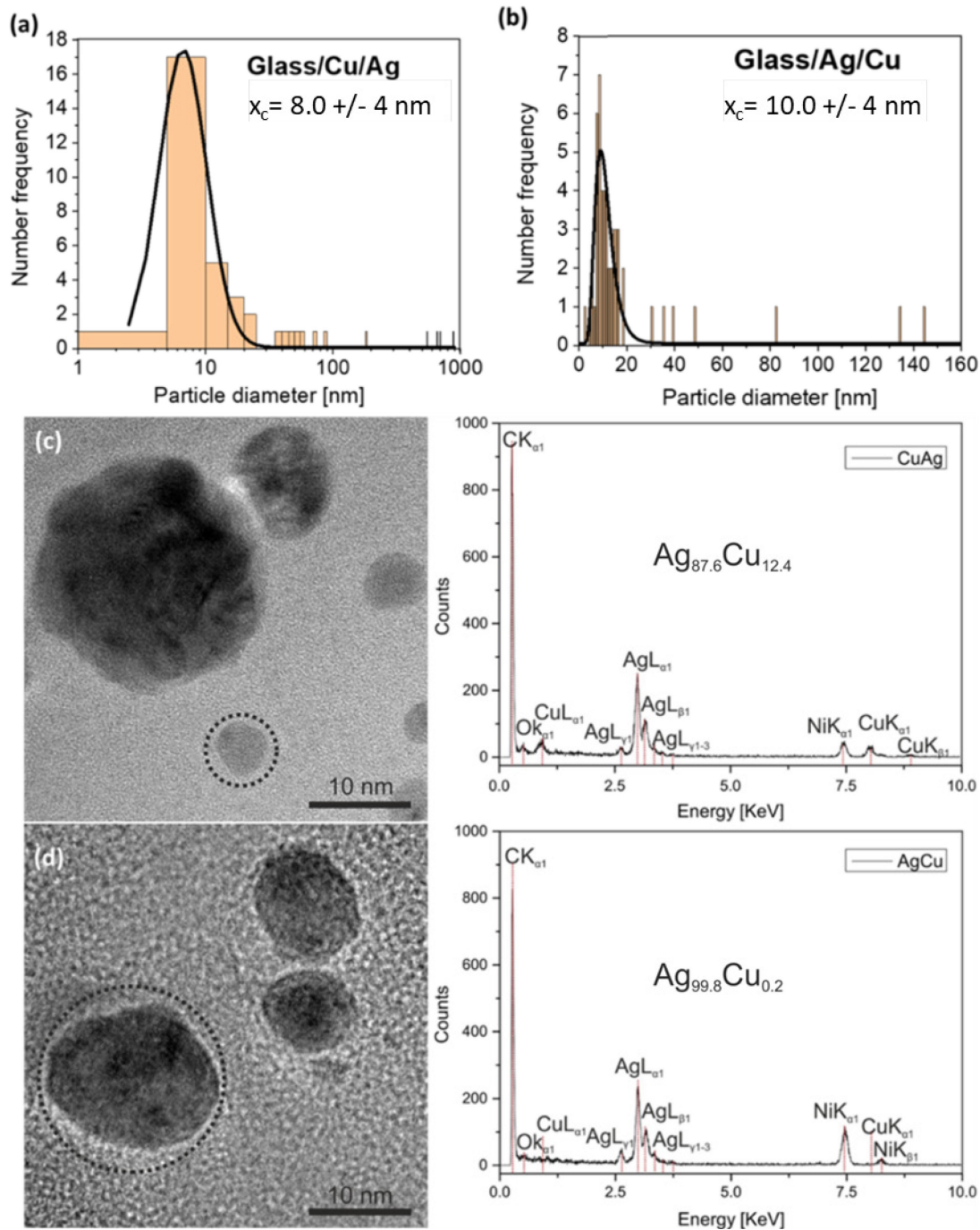


**Figure 15. (a), (b):** Number-weighted size distributions of nanoparticles generated from glass/Cu/Ag (a) and glass/Ag/Cu (b) layered targets, characterized via TEM images. Note the logarithmic scale used for the  $x$ -axis in (a) to enable an adequate representation of the wide range of measured nanoparticle diameters. The average diameters  $x_c$  listed in (a) and (b) are median values calculated from log-normal fitting curves of the number-weighted size distributions, and the error values are standard deviations from the log-normal fitting. The distributions are generated based on the evaluation of 40 and 52 nanoparticles for glass/Cu/Ag and glass/Ag/Cu, respectively. The bin size in all distributions is 5 nm. (c), (d): TEM bright-field images and corresponding EDX spectra, measured for exemplary nanoparticles marked on the TEM images. The exemplary nanoparticle generated from the glass/Ag/Cu target (c) has a composition of 87.6 at.% Ag and 12.4 at.% Cu. The exemplary nanoparticle generated from the glass/Cu/Ag target (d) has a composition of 99.8 at.% Ag and 0.2 at.% Cu. Carbon and Nickel signals arise from the TEM grid. It is, furthermore, unclear whether oxygen signals arise from the target or the nanoparticles.

The observation of larger nanoparticles in the experiments as compared to the ones predicted in the simulations can be explained by a combination of several factors. Firstly, the films used in the experiments are four times thicker than those considered in the simulations. According to the simulations, the large droplets originate from the decomposition of a transient hot metal layer generated at the water plume interface through the accumulation of the front part of the ablation plume. The ablation of a thicker film can be expected to produce a thicker and more stable interfacial layer, which would yield much larger droplets through a slower process of the interfacial layer decomposition.<sup>98</sup> Secondly, the formation of larger droplets may happen at a later stage of the ablation process through the coalescence of smaller liquid droplets. The concentration of the large droplets in the upper part of the expanding cavitation bubble (Figures 4 and 7) and the relatively low rate of cooling of these droplets are the computational predictions that favor the notion of long-term nanoparticle growth through the coalescence of smaller droplets. Finally, some of the largest nanoparticles observed in the experiments, particularly the ones with diameters approaching the micrometer scale, are likely to have the same origin as the large frozen droplets and pieces of debris observed in the SEM images shown in Figure 14a,c,e,f. As discussed in Section 3.4, these particles are likely to form through the disintegration of a molten film separated/spalled from the substrate in the periphery of the ablation spot, where the energy deposited by the laser pulse is not sufficient for inducing the phase explosion. Note that the volume of a single spherical particle with a diameter of 1  $\mu\text{m}$  corresponds to the volume of a disc of the original  $\sim 80$  nm-thick film with a diameter of about 2.9  $\mu\text{m}$ . The diameter of the ablation spot produced in the single-pulse ablation experiments is about 60  $\mu\text{m}$  (Figure 14), which suggests that the peripheral area experiencing melting and spallation can be sufficiently large to account for the large particles observed in the SEM images.

The nanoparticles were further analyzed by EDX spectroscopy to determine particle compositions on a single particle level. In this context, 40 and 52 individual particles were analyzed for the glass/Cu/Ag and the glass/Ag/Cu target arrangements, respectively. Figure 15c,d depict TEM images and EDX spectra for two exemplary nanoparticles: a  $\sim 5$  nm nanoparticle composed of 87.6 at.% Ag and 12.4 at.% Cu (Figure 15c) and a  $\sim 15$  nm nanoparticle composed of 99.8 at.% Ag and 0.2 at.% Cu (Figure 15d). The quantitative correlations between composition, particle number, and atomic abundance (proportional to mass) from single-particle EDX measurements are shown in Figure 16.

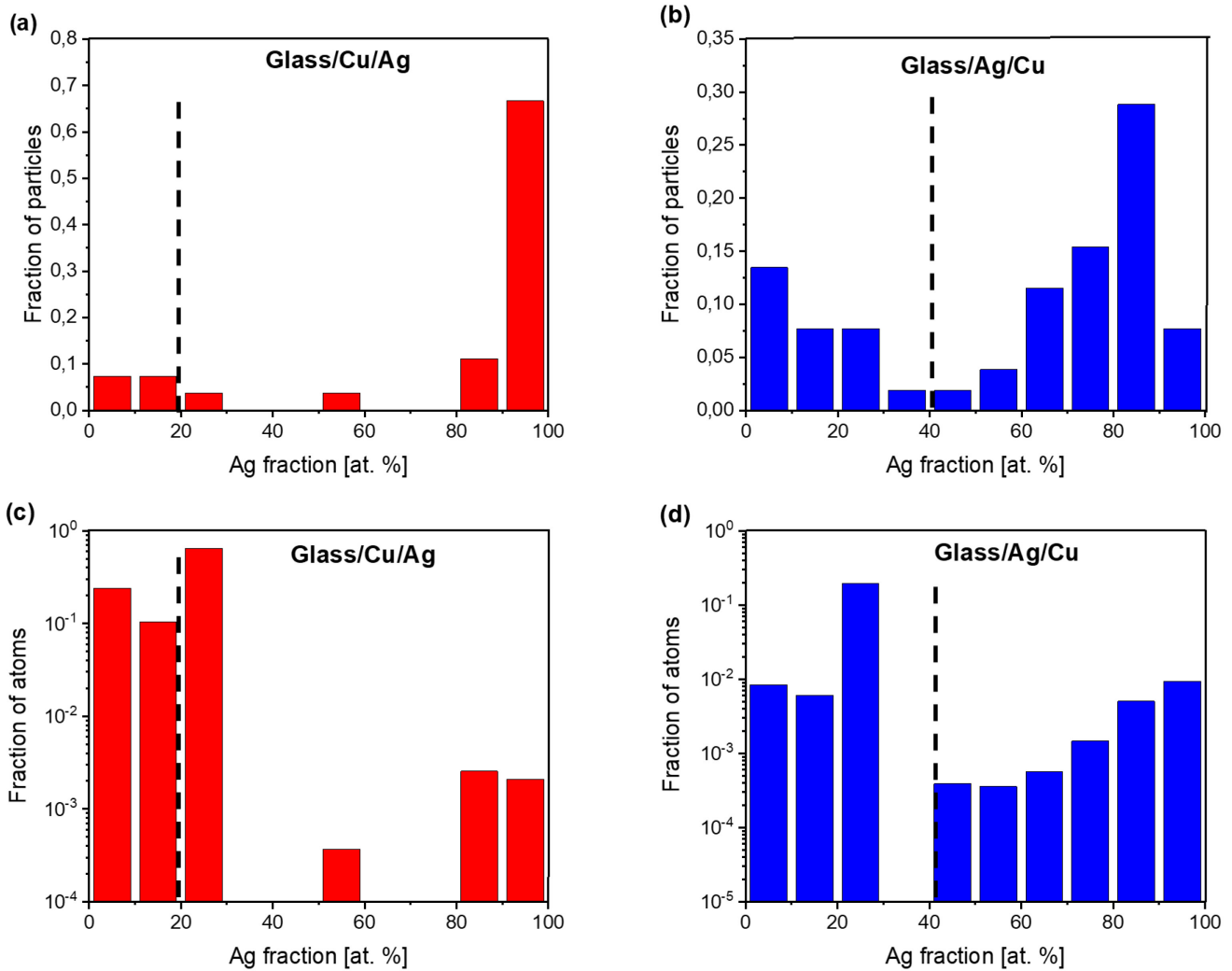


**Figure 16.** Fraction of nanoparticles (a,b) and fraction of atoms (c,d) in correlation with composition obtained for nanoparticles generated from glass/Cu/Ag, (a,c) and glass/Ag/Cu (b,d) bilayer targets. Logarithmic scale is used for the fraction of atoms to provide an adequate representation of the large contribution of Cu-rich particles. The distributions are generated based on EDX single particle analysis of 40 and 52 nanoparticles for glass/Cu/Ag and glass/Ag/Cu targets, respectively. The dashed lines represent the nominal molar fractions of the bilayer targets.

The analysis of the nanoparticle composition distributions reveals the apparent absence of the complete mixing of the two components present in the target films. The distributions exhibit an increased abundance of Ag-rich and Cu-rich nanoparticles, while the nanoparticles of intermediate compositions (which would represent the nominal target composition) are present at substantially lower numbers. The fact that the intermediate compositions are under-represented in the distributions is in a good agreement with the results of the simulations reported in Section 3.1-3.3, where the limited mixing of the two components at the initial dynamic/explosive stage of the ablation process is observed and related to the ablation mechanisms. Indeed, while the direct quantitative comparison of the computational and experimental distributions shown in Figures 11 and 16, respectively, is hampered by the limited timescale accessible for the atomistic modeling, the depletion of the central part of the distributions is apparent in both figures. The small and numerous nanoparticles with compositions dominated by

the lower layer component, observed in the simulations, Figure 11a, can be expected to grow in size and decrease in numerosity, bringing these parts of the distributions closer to the experimental ones.

The comparison of the experimental distributions of the fraction of nanoparticles and fraction of atoms with respect to the nanoparticle compositions, shown for the glass/Ag/Cu system in Figure 16b,d, points to the presence of smaller in numbers but relatively large Cu-rich nanoparticles. This observation is also consistent with the computational prediction of the formation of large nanoparticles enriched with the top component through the decomposition of the interfacial layer, see Figures 11b and 12. The clear dominance of the Cu-rich nanoparticles in the Ag on Cu case (Figure 16c), however, cannot be explained by the computational results, and is probably associated with only a few but mass (atom number) dominant larger particles with high copper content. The disproportionally large contribution of Cu-rich nanoparticles to the mass-weighted composition distributions, regardless of the layer arrangement in the bilayer targets, Figure 16c,d, is also reflected in the anomalously high total concentration of Cu in the nanoparticles. The Cu:Ag atom ratio evaluated for the whole ensemble of nanoparticles subjected to EDX analysis is 7 for the glass/Cu/Ag system and 5 for the glass/Ag/Cu system. This finding cannot be fully explained based on the dominance of Cu to the composition of the bilayer targets (80.4 at.% Cu in glass/Ag/Cu and 59.2 at.% Cu in glass/CuAg) and is probably an artifact of the low total number of analyzed particles.

Despite the differences between the experimental and computational distributions of nanoparticle compositions, the common conclusion on the limited mixing between the two components of the bilayer film suggests that the processes occurring during the first nanoseconds of ultrashort pulse laser ablation are playing a critical role in defining the final composition of the nanoparticles probed in the experiments. The results of this study complement and explain previous findings, which indicate that the formation of bimetallic nanoparticles by laser ablation in liquids is primarily controlled by the elemental segregation in the target and by the laser pulse duration. For ablation conducted with nanosecond pulses, the time scales of the plasma plume formation overlap with the pulse duration, leading to further heating of the plume, increase in the plasma temperature, and prolongation of the plasma lifetime.<sup>102,103</sup> Under these conditions, better elemental mixing can be expected prior to the particle formation, and predominantly bimetallic particles are obtained, even though they can differentiate into biphasic or core-shell morphologies in correlation with nominal nanoparticle composition.<sup>33</sup> This expectation has been experimentally confirmed for bulk alloy targets from other bimetallic systems,<sup>21,22</sup> as well as for FeAu<sup>23</sup> and AgAu<sup>24</sup> thin films. The effect of the pulse duration on the nanoparticle formation from thin-film targets with an overall composition of Fe<sub>50</sub>Au<sub>50</sub> was recently examined in Ref. 12, where a higher abundance of bimetallic FeAu core-shell nanoparticles (> 90% by mass) was observed in the case the bilayer targets ablated by nanosecond pulses. This is a clear indication of a pronounced atomic mixing and particle formation under thermodynamic control, as in this system, a segregated core-shell morphology is the most stable structure predicted by the bulk

phase diagram and the surface energy model. In the case of picosecond pulsed ablation, on the other hand, the Fe-Au core-shell nanoparticles were less frequently found, probably due to the enrichment of nanoparticles with gold, which prevents the formation of the core-shell structure.<sup>32</sup> In another study,<sup>104</sup> the alloy nanoparticles produced by picosecond laser ablation of mixed and pressed micropowder Mn/Ni and Co/Fe targets were examined. In both cases, the nanoparticle yield primarily consisted of single element nanoparticles or particles with pronounced enrichment of one of the components, even though the number of target's microparticle grains within one laser spot was between 27,000 and 270,000. Only upon heat treatment of the target, which induces sintering, diffusion, and alloying in the partially miscible Mn/Ni and Co/Fe systems, consecutive picosecond laser ablation yielded alloy nanoparticles with compositions in good accordance with the nominal target composition. These findings are consistent with the results reported in the present paper and suggest that, in case of ultrashort pulse laser ablation of targets with spatial separation of the components, such as multilayer films or consolidated micropowder-based materials, the atomic mixing in the ablation plume is limited and the composition of the nanoparticles generated by laser ablation in liquids can significantly deviate from the nominal composition of the target.

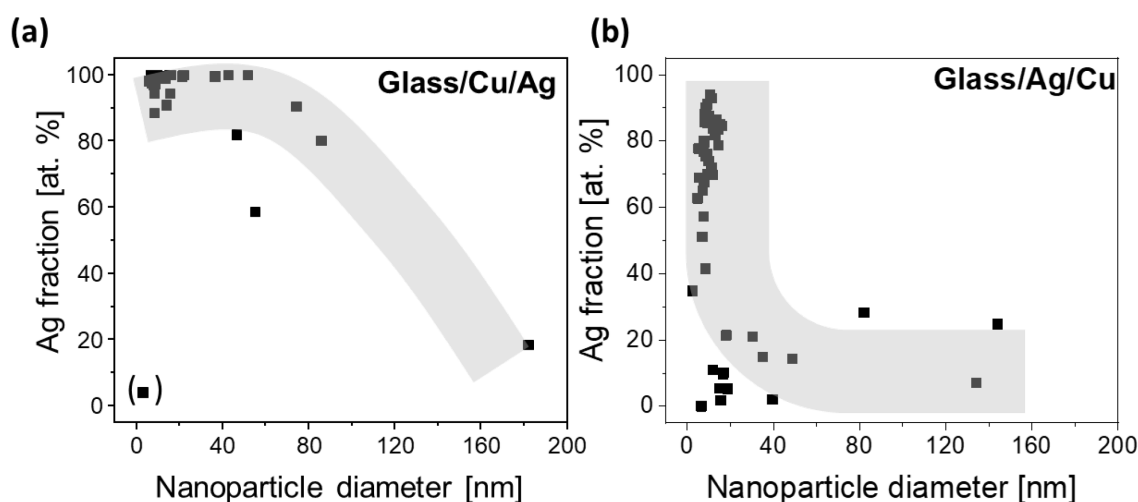


**Figure 17.** The distribution of nanoparticles by diameter and composition determined in experiments performed for the glass/Cu/Ag (a) and the glass/Ag/Cu (b) layer stacking. The shaded areas are added as a guide to the eye and do not represent any mathematical model fit. The dot in brackets in (a) indicates one particle found in the whole sample with a diameter of 2 nm, which, in contrast to the general trend, is almost completely made of Cu. As statements based on a single particle are not statistically useful, the point is excluded from the interpretation.

Finally, the EDX data and TEM size histograms were combined to establish a correlation between particle diameter and atomic composition (Figure 17). These data clearly show that large particles, particularly those exceeding 100 nm, are predominantly copper-rich, while small particles are silver-rich. This general rule seems to apply independently of the layer arrangement. The transition from Ag-rich small nanoparticles to larger Cu-rich particles, however, occurs within different ranges of nanoparticle diameters. For the glass/Ag/Cu bilayer target, the transition happens in a very narrow range of nanoparticle diameters around 10 nm, with all

nanoparticles larger than 16-17 nm having Cu as the major component. For the glass/Cu/Ag bilayer, the transition is more gradual and occurs as the nanoparticle diameter increases from 40 to 90 nm.

The shift of the transition from Ag-rich to Cu-rich nanoparticles to larger nanoparticle sizes observed for the glass/Cu/Ag bilayer target can be related to the computational prediction of the formation of nanoparticles in the size range of 10 to 50 nm from the top layer of the bilayer target at the initial stage of the ablation process. These nanoparticles, originating from decomposition of the transient interfacial layer formed at the front of the ablation plume, are Ag-rich in case Ag is in the top layer and Cu-rich for the inverse target arrangement. The contribution of these nanoparticles may be responsible for the appearance of the medium-sized Ag-rich nanoparticles in the distribution shown in Figure 17a for the glass/Cu/Ag target. The same mechanisms are predicted to produce Cu-rich nanoparticles in the case of the glass/Ag/Cu target, which may be related to the sharp size dependence of the nanoparticle composition observed for this system in Figure 17b.

As discussed above, we currently do not have a clear explanation for the strong dominance of Cu in the largest particles and in the overall composition of all the nanoparticles analyzed in the experiments. The large copper-rich nanoparticles with diameters exceeding 100 nm may originate from later stages of the particle formation process, could be the products of post-irradiation processes, or may even be artifacts of the TEM sample preparation process. Similarly, the pronounced dominance of Ag in the composition of small nanoparticles regardless of the arrangement of the two layers in the bilayer target cannot be explained based on the simulation results and is likely to be defined by the longer-term processes contributing to the nanoparticle formation. In particular, the lower surface energy of Ag as compared to Cu and the tendency of Ag to segregate to the surface of alloy nanoparticles<sup>105</sup> may facilitate the growth of Cu-rich nanoparticles through condensation in the cavitation bubble at low levels of metal vapor supersaturation.

To recap the conclusions of the experimental part of this study, the experimental findings on the Au-Cu nanoparticles generated by ultrafast laser ablation of bilayer targets in a liquid environment confirm the key predictions of the atomistic simulations, namely: i) the presence of large nanoparticles with diameters significantly exceeding the total thickness of the film targets, and ii) the “splitting” of the nanoparticle compositions into Cu-rich and Ag-rich fractions with only a minor population of Ag-Cu nanoparticles with equimolar composition.

#### **4. Conclusions**

The results of a joint computational and experimental study of the nanoparticle formation in ultrashort PLAL of Ag-Cu bilayer films provide clear evidence of a limited mixing between the two components of the bilayer films. The distributions of nanoparticle compositions predicted in large-scale atomistic simulations and obtained through EDX probing of individual nanoparticles exhibit an enhanced abundance of Ag-rich and Cu-

rich nanoparticles, while the nanoparticles of intermediate compositions are present at substantially lower numbers. The observation that the nanoscale spatial separation of the two components in the bilayer films can manifest itself in the sharp departure from the complete mixing in the compositions of colloidal nanoparticles generated by PLAL is surprising, particularly given the fact that the ablation is performed in the regime of phase explosion and the bilayers have thicknesses of only a few tens of nm. Indeed, according to the conventional picture of the nanoparticle formation in PLAL, the explosive decomposition of the entire bilayer target into vapor, atomic clusters, and small droplets should be followed by microsecond-scale expansion of the cavitation bubble, gradual cooling of the ablation plume mixed with vapor originating from the liquid environment, and eventual nucleation and growth of the nanoparticles. This scenario does not leave any possibility for the limited mixing, since the vapor phase mixing is fast and would be complete within the expanding cavitation bubble. Consequently, this work provides fundamentally new insight into particle formation by PLAL using ultrashort pulsed laser and targets with defined elemental segregation.

The results of large-scale atomistic simulations of ultrashort PLAL of metal bilayers in water, however, reveal a more complicated multistep picture of the initial dynamic stage of the ablation process, which involves the rapid formation of nanoparticles of different sizes and compositions in different parts of the emerging cavitation bubble. In particular, the simulations predict that the ablation plume (a hot mixture of metal vapor, atomic clusters, and liquid droplets generated in the phase explosion of the superheated film) is rapidly decelerated by the resistance from the water environment and accumulates at the water-plume interface. The accumulation of the ablation plume at the interface with water leads to the formation of a relatively dense hot metal layer, which heats the adjacent water and brings it to the supercritical state. The expansion of the supercritical water and active evaporation of hot metal create a low-density metal-water mixing region with thermodynamic conditions suitable for condensation of metal atoms into clusters, growth of the atomic clusters into nanoparticles, as well as rapid cooling and crystallization of the nanoparticles. The interfacial layer itself is destabilized/roughened by the dynamic interaction with water (rapid cooling and Rayleigh-Taylor instability) and decomposes into large droplets on the timescale of nanoseconds.

The complex dynamics of the initial stage of the ablation process, briefly outlined above, has direct implications on the composition of the nanoparticles generated in different parts of the emerging cavitation bubble. The formation of the transient interfacial layer creates a barrier hampering the mixing of the lower part of the ablation plume, mostly consisting of the component originating from the lower layer of the bilayer target, with the upper part of the plume interacting with water and largely consisting of the component originating from the top layer of the bilayer film. As a result, the small nanoparticles formed through the nucleation and growth at the front of the bubble, in the water-plume mixing region, consist almost exclusively of the top layer component, whereas the nanoparticles closest to the substrate have compositions of an almost pure component of the lower

layer of the bilayer targets. The composition of large nanoparticles generated through the decomposition of the interfacial layer is dominated by the top layer component, but includes a substantial minority contribution from the lower layer component, particularly in the case of the largest droplets formed in the lower part of the interfacial layer.

While the direct projection of the computational predictions to the final characteristics of colloidal nanoparticles generated in PLAL experiments is hampered by the short timescale accessible for the atomistic modeling, the observation that a large number of nanoparticles are already formed during the first nanoseconds of the ablation process suggests that the longer-term processes of nanoparticle growth and coalescence are unlikely to eliminate the compositional disbalance predicted in the simulations. Indeed, the distributions of nanoparticle compositions obtained in the experiments exhibit an increased abundance of Ag-rich and Cu-rich nanoparticles, while the nanoparticles of intermediate compositions are present at substantially lower numbers. Hence, the experiments clearly validate the computational prediction on the limited elemental mixing in nanoparticles when a segregated target is ablated by ultrashort pulses in a liquid environment.

Some of the characteristics of the experimental distributions, such as the pronounced tendency of the largest particles to be enriched with Cu and the dominance of Ag in the composition of small nanoparticles regardless of the arrangement of the two layers in the bilayer target cannot be explained based on the simulation results and are likely to be defined by longer-term processes occurring closer to the conditions of local thermodynamic equilibrium and sensitive to the relatively small but noticeable differences in the thermodynamic properties of Cu and Ag, such as lower surface energy of Ag and its tendency to segregate to the surface of alloy nanoparticles. Note that the choice of the spatial order of Cu and Ag in the bilayer target does not alter the overall picture of the initial stage of the ablation process revealed in the simulations, although some quantitative differences are observed and attributed to the substantial difference in the strength of the electron-phonon coupling in the two materials.

In addition to the limited mixing of the two components, another experimental observation that does agree with the modeling results but does not fit well with the conventional picture of PLAL is the presence of nanoparticles that are much larger than the thickness of the target film. The nanoparticles in the size range of a hundred of nanometers or larger can hardly form through the condensation from the vapor phase and cannot appear as a direct product of the explosive disintegration of the irradiated thin film. While some of the largest nanoparticles observed in the experiments, particularly the ones with diameters approaching the micron scale, are likely to form through the fragmentation of a molten film spalled from the substrate in the periphery of the irradiated spot, the computational results suggest an alternative scenario. The simulations predict that, despite the strong superheating and complete explosive disintegration of the irradiated film, the large nanoparticles can

promptly form through the accumulation of the ablation plume at the interface with the liquid environment followed by disintegration of the interfacial layer.

The results reported in this paper have practical implications for the generation of multicomponent nanoparticles by ultrashort PLAL. The complex dynamic interaction of the ablation plume with liquid environment, occurring at the initial stage of the ablation process, breaks down the intuitive assumptions on the complete mixing of the components separated in the bilayer target by only tens of nanometers and on the direct connection between the maximum size of the nanoparticles and thickness of the thin film target. Hence, from a practical point of view, single-pulse ultrashort PLAL of a phase-separated multicomponent target cannot be expected to produce a major fraction of alloy nanoparticles with compositions closely matching the nominal composition of the target. The utilization of nanosecond pulses and multi-pulse irradiation of emerging colloidal solution of nanoparticles could result in a better mixing of the elements, and could be advantageous for the fabrication of alloy nanoparticles from targets that are not perfectly pre-mixed on the nanoscale. On the other hand, in upscaled PLAL,<sup>106</sup> ultrashort pulse durations are the better choice when working in organic liquids, as the nanosecond pulses cause stronger heating and a larger extent of bubble formation attenuating productivity. Further well-integrated computational and experimental efforts are required to fully understand the complex mechanisms of PLAL and to enable the design of nanoparticle production methods that would balance the ever-increasing demand for productivity with the need to ensure precise control over nanoparticle size and composition.

## **Associated Content**

### **Supporting Information**

The Supporting Information is available free of charge on the ACS Publications website at DOI: ...

Animated sequences of snapshots from the simulations discussed in this paper, with atoms colored by atom type and potential energy. The animations are provided in animated GIF format and as AVI movies.

### **Acknowledgements**

Financial support for this work was provided by the National Science Foundation (NSF) through Grant CMMI-1663429 and DMR-1610936. Furthermore, we acknowledge the Deutsche Forschungsgemeinschaft for financial support within projects BA 3580/18-1 and KI 1263/15-1. Computational support was provided by the NSF through the Extreme Science and Engineering Discovery Environment (project TGDMR110090). L. V. Z. acknowledges the Mercator Fellowship at the University of Duisburg-Essen, Germany, funded by Deutsche Forschungsgemeinschaft (BA 3580/22-1). We further thank Dr. Kateryna Loza, Dr. Detlef Spoddig and Ruksan Nadarajah (University of Duisburg-Essen) for assistance with SEM and EDX measurements of targets and ablation spots.

## References

1. Reichenberger, S.; Marzun, G.; Muhler, M.; Barcikowski, S. Perspective of surfactant-free colloidal nanoparticles in heterogeneous catalysis. *ChemCatChem* **2019**, *11*, 4489-4518.
2. Zhang, J. M.; Chaker, M.; Ma, D. L. Pulsed laser ablation based synthesis of colloidal metal nanoparticles for catalytic applications. *J. Colloid Interface Sci.* **2017**, *489*, 138-149.
3. Rehbock, C.; Jakobi, J.; Gamrad, L.; van der Meer, S.; Tiedemann, D.; Taylor, U.; Kues, W.; Rath, D.; Barcikowski, S. Current state of laser synthesis of metal and alloy nanoparticles as ligand-free reference materials for nano-toxicological assays. *Beilstein J. Nanotechnol.* **2014**, *5*, 1523-1541.
4. Dakal, T. C.; Kumar, A.; Majumdar, R. S.; Yadav, V. Mechanistic basis of antimicrobial actions of silver nanoparticles. *Front. Microbiol.* **2016**, *7*, 1831.
5. Ingle, A. P.; Duran, N.; Rai, M. Bioactivity, mechanism of action, and cytotoxicity of copper-based nanoparticles: A review. *Appl. Microbiol. Biotechnol.* **2014**, *98*, 1001-1009.
6. Ma, M.; Trzesniewski, B. J.; Xie, J.; Smith, W. A. Selective and efficient reduction of carbon dioxide to carbon monoxide on oxide-derived nanostructured silver electrocatalysts. *Angew. Chem. Int. Ed.* **2016**, *55*, 9748-9752.
7. Mendez-Medrano, M. G.; Kowalska, E.; Lehoux, A.; Herissan, A.; Ohtani, B.; Bahena, D.; Briois, V.; Colbeau-Justin, C.; Rodriguez-Lopez, J. L.; Remita, H. Surface modification of TiO<sub>2</sub> with Ag nanoparticles and CuO nanoclusters for application in photocatalysis. *J. Phys. Chem. C* **2016**, *120*, 5143-5154.
8. Subramanian, P. R.; Perepezko, J. H. The Ag-Cu (silver-copper) system. *J. Phase Equilib.* **1993**, *14*, 62-75.
9. Kim, N. R.; Shin, K.; Jung, I.; Shim, M.; Lee, H. M. Ag-Cu bimetallic nanoparticles with enhanced resistance to oxidation: A combined experimental and theoretical study. *J. Phys. Chem. C* **2014**, *118*, 26324-26331.
10. Riabinina, D.; Chaker, M.; Margot, J. Dependence of gold nanoparticle production on pulse duration by laser ablation in liquid media. *Nanotechnology* **2012**, *23*, 135603.
11. Kabashin, A. V.; Meunier, M. Synthesis of colloidal nanoparticles during femtosecond laser ablation of gold in water. *J. Appl. Phys.* **2003**, *94*, 7941-7943.
12. Tymoczko, A.; Kamp, M.; Rehbock, C.; Kienle, L.; Cattaruzza, E.; Barcikowski, S.; Amendola, V. One-step synthesis of Fe-Au core-shell magnetic-plasmonic nanoparticles driven by interface energy minimization. *Nanoscale Horiz.* **2019**, *4*, 1326-1332.
13. Zhang, D.; Gökce, B.; Barcikowski, S. Laser synthesis and processing of colloids: Fundamentals and applications. *Chem. Rev.* **2017**, *117*, 3990-4103.
14. Wagener, P.; Jakobi, J.; Rehbock, C.; Chakravadhanula, V. S. K.; Thede, C.; Wiedwald, U.; Bartsch, M.; Kienle, L.; Barcikowski, S. Solvent-surface interactions control the phase structure in laser-generated iron-gold core-shell nanoparticles. *Sci. Rep.* **2016**, *6*, 23352.
15. Moradi, M.; Solati, E.; Darvishi, S.; Dorrnian, D. Effect of aqueous ablation environment on the characteristics of ZnO nanoparticles produced by laser ablation. *J. Clust. Sci.* **2016**, *27*, 127-138.
16. Chaturvedi, A.; Joshi, M. P.; Mondal, P.; Sinha, A. K.; Srivastava, A. K. Growth of anatase and rutile phase TiO<sub>2</sub> nanoparticles using pulsed laser ablation in liquid: Influence of surfactant addition and ablation time variation. *Appl. Surf. Sci.* **2017**, *396*, 303-309.
17. Sylvestre, J. P.; Poulin, S.; Kabashin, A. V.; Sacher, E.; Meunier, M.; Luong, J. H. T. Surface chemistry of gold nanoparticles produced by laser ablation in aqueous media. *J. Phys. Chem. B* **2004**, *108*, 16864-16869.

18. Merk, V.; Rehbock, C.; Becker, F.; Hagemann, U.; Nienhaus, H.; Barcikowski, S. In situ non-DLVO stabilization of surfactant-free, plasmonic gold nanoparticles: Effect of Hofmeister's anions. *Langmuir* **2014**, *30*, 4213-4222.
19. Pfeiffer, C.; Rehbock, C.; Hühn, D.; Carrillo-Carrion, C.; de Aberasturi, D. J.; Merk, V.; Barcikowski, S.; Parak, W. J. Interaction of colloidal nanoparticles with their local environment: the (ionic) nanoenvironment around nanoparticles is different from bulk and determines the physico-chemical properties of the nanoparticles. *J. R. Soc. Interface* **2014**, *11*, 20130931.
20. Amendola, V.; Amans, D.; Ishikawa, Y.; Koshizaki, N.; Scirè, S.; Compagnini, G.; Reichenberger, S.; Barcikowski, S. Room-temperature laser synthesis in liquid of oxide, metal-oxide core-shells and doped oxide nanoparticles. *Chem. Eur. J.* **2020**, *26*, 9206-9242.
21. Neumeister, A.; Jakobi, J.; Rehbock, C.; Moysig, J.; Barcikowski, S. Monophasic ligand-free alloy nanoparticle synthesis determinants during pulsed laser ablation of bulk alloy and consolidated microparticles in water. *Phys. Chem. Chem. Phys.* **2014**, *16*, 23671-23678.
22. Zhang, J. M.; Oko, D. N.; Garbarino, S.; Imbeault, R.; Chaker, M.; Tavares, A. C.; Guay, D.; Ma, D. L. Preparation of PtAu alloy colloids by laser ablation in solution and their characterization. *J. Phys. Chem. C* **2012**, *116*, 13413-13420.
23. Amendola, V.; Scaramuzza, S.; Carraro, F.; Cattaruzza, E. Formation of alloy nanoparticles by laser ablation of Au/Fe multilayer films in liquid environment. *J. Colloid Interface Sci.* **2017**, *489*, 18-27.
24. Nastulyavichus, A. A.; Kudryashov, S. I.; Smirnov, N. A.; Rudenko, A. A.; Kharin, A. Y.; Busleev, N. I.; Zayarny, D. A.; Ionin, A. A.; Kirilenko, D. A.; Brunkov, P. N. Novel approach of controllable stoichiometric fabrication of alloyed Au/Ag nanoparticles by nanosecond laser ablation of thin bi-layered films in water. *Laser Phys. Lett.* **2019**, *16*, 096002.
25. Bubb, D. M.; O'Malley, S. M.; Schoeffling, J.; Jimenez, R.; Zinderman, B.; Yi, S. Size control of gold nanoparticles produced by laser ablation of thin films in an aqueous environment. *Chem. Phys. Lett.* **2013**, *565*, 65-68.
26. Scaramuzza, S.; Zerbetto, M.; Amendola, V. Synthesis of gold nanoparticles in liquid environment by laser ablation with geometrically confined configurations: Insights to improve size control and productivity. *J. Phys. Chem. C* **2016**, *120*, 9453-9463.
27. Jakobi, J.; Menendez-Manjon, A.; Chakravadhanula, V. S. K.; Kienle, L.; Wagener, P.; Barcikowski, S. Stoichiometry of alloy nanoparticles from laser ablation of PtIr in acetone and their electrophoretic deposition on PtIr electrodes. *Nanotechnology* **2011**, *22*, 145601.
28. Oko, D. N.; Garbarino, S.; Zhang, J. M.; Xu, Z. M.; Chaker, M. H.; Ma, D. L.; Guay, D.; Tavares, A. C. Dopamine and ascorbic acid electro-oxidation on Au, AuPt and Pt nanoparticles prepared by pulse laser ablation in water. *Electrochim. Acta* **2015**, *159*, 174-183.
29. Amendola, V.; Meneghetti, M.; Bakr, O. M.; Riello, P.; Polizzi, S.; Anjum, D. H.; Fiameni, S.; Arosio, P.; Orlando, T.; Fernandez, C. D.; *et al.* Coexistence of plasmonic and magnetic properties in Au<sub>89</sub>Fe<sub>11</sub> nanoalloys. *Nanoscale* **2013**, *5*, 5611-5619.
30. Amendola, V.; Scaramuzza, S.; Agnoli, S.; Granozzi, G.; Meneghetti, M.; Campo, G.; Bonanni, V.; Pineider, F.; Sangregorio, C.; Ghigna, P.; *et al.* Laser generation of iron-doped silver nanotruffles with magnetic and plasmonic properties. *Nano Res.* **2015**, *8*, 4007-4023.
31. Amendola, V.; Scaramuzza, S.; Agnoli, S.; Polizzi, S.; Meneghetti, M. Strong dependence of surface plasmon resonance and surface enhanced Raman scattering on the composition of Au-Fe nanoalloys. *Nanoscale* **2014**, *6*, 1423-1433.

32. Tymoczko, A.; Kamp, M.; Prymak, O.; Rehbock, C.; Jakobi, J.; Schürmann, U.; Kienle, L.; Barcikowski, S. How the crystal structure and phase segregation of Au-Fe alloy nanoparticles are ruled by the molar fraction and size. *Nanoscale* **2018**, *10*, 16434-16437.
33. Malviya, K. D.; Chattopadhyay, K. Synthesis and mechanism of composition and size dependent morphology selection in nanoparticles of Ag-Cu alloys processed by laser ablation under liquid medium. *J. Phys. Chem. C* **2014**, *118*, 13228-13237.
34. Petrovic, S.; Salatic, B.; Milovanovic, D.; Lazovic, V.; Zivkovic, L. J.; Trtica, M.; Jelenkovic, B. Agglomeration in core-shell structure of CuAg nanoparticles synthesized by the laser ablation of Cu target in aqueous solutions. *J. Opt.* **2015**, *17*, 025402.
35. Malviya, K. D.; Chattopadhyay, K. Temperature- and size-dependent compositionally tuned microstructural landscape for Ag-46 atom % Cu nanoalloy prepared by laser ablation in liquid. *J. Phys. Chem. C* **2016**, *120*, 27699-27706.
36. Tarasenko, N.; Nominé, A.; Nevar, A.; Nedelko, M.; Kabbara, H.; Bruyère, S.; Ghanbaja, J.; Noel, C.; Krasilin, A.; Zograf, G.; *et al.* Synergistic effect of plasma and laser processes in liquid for alloyed-nanoparticle synthesis. *Phys. Rev. Appl.* **2020**, *13*, 014021.
37. Malviya, K. D.; Srivastava, C.; Chattopadhyay, K. Phase formation and stability of alloy phases in free nanoparticles: some insights. *RSC Adv.* **2015**, *5*, 35541-35550.
38. Kamp, M.; Tymoczko, A.; Schürmann, U.; Jakobi, J.; Rehbock, C.; Rätzke, K.; Barcikowski, S.; Kienle, L. Temperature-dependent ultrastructure transformation of Au-Fe nanoparticles investigated by in situ scanning transmission electron microscopy. *Cryst. Growth Des.* **2018**, *18*, 5434-5440.
39. Povarnitsyn, M. E.; Itina, T. E. Hydrodynamic modeling of femtosecond laser ablation of metals in vacuum and in liquid. *Appl. Phys. A* **2014**, *117*, 175-178.
40. Shih, C.-Y.; Shugaev, M. V.; Wu, C.; Zhigilei, L. V. Generation of subsurface voids, incubation effect, and formation of nanoparticles in short pulse laser interactions with bulk metal targets in liquid: Molecular dynamics study. *J. Phys. Chem. C* **2017**, *121*, 16549-16567.
41. Petrov, Yu. V.; Khokhlov, V. A.; Zhakhovsky, V. V.; Inogamov, N. A. Hydrodynamic phenomena induced by laser ablation of metal into liquid. *Appl. Surf. Sci.* **2019**, *492*, 285-297.
42. Inogamov, N. A.; Khokhlov, V. A.; Petrov, Yu. V.; Zhakhovsky, V. V. Hydrodynamic and molecular-dynamics modeling of laser ablation in liquid: from surface melting till bubble formation. *Opt. Quantum Electron.* **2020**, *52*, 63.
43. Itina, T. E. On nanoparticle formation by laser ablation in liquids. *J. Phys. Chem. C* **2011**, *115*, 5044-5048.
44. Povarnitsyn, M. E.; Itina, T. E.; Levashov, P. R.; Khishchenko, K. V. Mechanisms of nanoparticle formation by ultra-short laser ablation of metals in liquid environment. *Phys. Chem. Chem. Phys.* **2013**, *15*, 3108-3114.
45. Shih, C.-Y.; Wu, C.; Shugaev, M. V.; Zhigilei, L. V. Atomistic modeling of nanoparticle generation in short pulse laser ablation of thin metal films in water. *J. Colloid Interface Sci.* **2017**, *489*, 3-17.
46. Shih, C.-Y.; Streubel, R.; Heberle, J.; Letzel, A.; Shugaev, M. V.; Wu, C.; Schmidt, M.; Gökce, B.; Barcikowski, S.; Zhigilei, L. V. Two mechanisms of nanoparticle generation in picosecond laser ablation in liquids: the origin of the bimodal size distribution. *Nanoscale* **2018**, *10*, 6900-6910.
47. Shih, C.-Y.; Shugaev, M. V.; Wu, C.; Zhigilei, L. V. The effect of pulse duration on nanoparticle generation in pulsed laser ablation in liquids: Insights from large-scale atomistic simulations. *Phys. Chem. Chem. Phys.* **2020**, *22*, 7077-7099.

48. Ivanov, D. S.; Izgin T.; Maiorov, A. N.; Veiko, V. P.; Rethfeld, B.; Dombrovska, Y. I.; Garcia, M. E.; Zvestovskaya, I. N.; Klimentov, S. M.; Kabashin, A. V. Numerical investigation of ultrashort laser-ablative synthesis of metal nanoparticles in liquids using the atomistic-continuum model. *Molecules* **2020**, *25*, 67.
49. Marzun, G.; Nakamura, J.; Zhang, X.; Barcikowski, S.; Wagener, P. Size control and supporting of palladium nanoparticles made by laser ablation in saline solution as a facile route to heterogeneous catalysts. *Appl. Surf. Sci.* **2015**, *348*, 75-84.
50. Reich, S.; Letzel, A.; Menzel, A.; Kretzschmar, N.; Gökce, B.; Barcikowski, S.; Plech, A. Early appearance of crystalline nanoparticles in pulsed laser ablation in liquids dynamics. *Nanoscale* **2019**, *11*, 6962-6969.
51. Shih, C.-Y.; Gnilitzkyi, I.; Shugaev, M. V.; Skoulas, E.; Stratakis, E.; Zhigilei, L. V. Effect of a liquid environment on single-pulse generation of laser induced periodic surface structures and nanoparticles. *Nanoscale* **2020**, *12*, 7674-7687.
52. Naghilou, A.; He, M.; Schubert, J. S.; Zhigilei, L. V.; Kautek, W. Femtosecond laser generation of microbumps and nanojets on single and bilayer Cu/Ag thin films. *Phys. Chem. Chem. Phys.* **2019**, *21*, 11846-11860.
53. Ivanov, D. S.; Zhigilei, L. V. Combined atomistic-continuum modeling of short-pulse laser melting and disintegration of metal films. *Phys. Rev. B* **2003**, *68*, 064114.
54. Zhigilei, L. V.; Lin, Z.; Ivanov, D. S. Atomistic modeling of short pulse laser ablation of metals: Connections between melting, spallation, and phase explosion. *J. Phys. Chem. C* **2009**, *113*, 11892-11906.
55. Wu, C.; Zhigilei, L. V. Microscopic mechanisms of laser spallation and ablation of metal targets from large-scale molecular dynamics simulations. *Appl. Phys. A* **2014**, *114*, 11-32.
56. Tabetah, M.; Matei, A.; Constantinescu, C.; Mortensen, N. P.; Dinescu, M.; Schou, J.; Zhigilei, L. V. The minimum amount of "matrix" needed for matrix-assisted pulsed laser deposition of biomolecules. *J. Phys. Chem. B* **2014**, *118*, 13290-13299.
57. Zou, J.; Wu, C.; Robertson, W. D.; Zhigilei, L. V.; Miller, R. J. D. Molecular dynamics investigation of desorption and ion separation following picosecond infrared laser (PIRL) ablation of an ionic aqueous protein solution. *J. Chem. Phys.* **2016**, *145*, 204202.
58. Karim, E. T.; Shugaev, M. V.; Wu, C.; Lin, Z.; Hainsey, R. F.; Zhigilei, L. V. Atomistic simulation study of short pulse laser interactions with a metal target under conditions of spatial confinement by a transparent overlayer. *J. Appl. Phys.* **2014**, *115*, 183501.
59. Anisimov, S. I.; Kapeliovich, B. L.; Perel'man, T. L. Electron emission from metal surfaces exposed to ultrashort laser pulses. *Sov. Phys. JETP* **1974**, *39*, 375-377.
60. Williams, P. L.; Mishin, Y.; Hamilton, J. C. An embedded-atom potential for the Cu–Ag system. *Modelling Simul. Mater. Sci. Eng.* **2006**, *14*, 817-833.
61. Gloor, G. J.; Jackson, G.; Blas, F. J.; de Miguel, E. Test-area simulation method for the direct determination of the interfacial tension of systems with continuous or discontinuous potentials. *J. Chem. Phys.* **2005**, *123*, 134703.
62. Shugaev, M. V.; Zhigilei, L. V. Thermodynamic analysis and atomistic modeling of subsurface cavitation in photomechanical spallation. *Comput. Mater. Sci.* **2019**, *166*, 311-317.
63. Ohse, R. W.; von Tippelskirch, H. The critical constants of the elements and of some refractory materials with high critical temperatures. (A Review). *High Temp-High Press* **1977**, *9*, 367-385.
64. Gadre, K. S.; Alford, T. L. Contact angle measurements for adhesion energy evaluation of silver and copper films on parylene-n and SiO<sub>2</sub> substrates. *J. Appl. Phys.* **2003**, *93*, 919-923.

65. Lin, Z.; Zhigilei, L. V.; Celli, V. Electron-phonon coupling and electron heat capacity of metals under conditions of strong electron-phonon nonequilibrium. *Phys. Rev. B* **2008**, *77*, 075133.
66. Wu, C.; Thomas, D. A.; Lin, Z.; Zhigilei, L. V. Runaway lattice-mismatched interface in an atomistic simulation of femtosecond laser irradiation of Ag film – Cu substrate system. *Appl. Phys. A* **2011**, *104*, 781-792.
67. Wellershoff, S.-S.; Hohlfeld, J.; Gudde, J.; Matthias, E. The role of electron–phonon coupling in femtosecond laser damage of metals. *Appl. Phys. A* **1999**, *69*, S99-S107.
68. Hohlfeld, J.; Wellershoff, S.-S.; Gudde, J.; Conrad, U.; Jahnke, V.; Matthias, E. Electron and lattice dynamics following optical excitation of metals. *Chem. Phys.* **2000**, *251*, 237-258.
69. Palik, E. D. *Handbook of Optical Constants of Solids*; Vol. **3**, Academic press: New York, 1998.
70. Bauerle, D. *Laser Processing and Chemistry*; Springer-Verlag: Berlin Heidelberg, 2000.
71. Shugaev, M. V.; He, M.; Levy, Y.; Mazzi, A.; Miotello, A.; Bulgakova, N. M.; Zhigilei, L. V. Laser-induced thermal processes: Heat transfer, generation of stresses, melting and solidification, vaporization and phase explosion. In *Handbook of Laser Micro- and Nano-Engineering*; Sugioka K., Ed., Springer: Cham, 2020.
72. Wu, C.; Christensen, M. S.; Savolainen, J.-M.; Balling, P.; Zhigilei, L. V. Generation of sub-surface voids and a nanocrystalline surface layer in femtosecond laser irradiation of a single crystal Ag target. *Phys. Rev. B* **2015**, *91*, 035413.
73. Byskov-Nielsen, J.; Savolainen, J.-M.; Christensen, M. S.; Balling, P. Ultra-short pulse laser ablation of copper, silver and tungsten: experimental data and two-temperature model simulations. *Appl. Phys. A* **2011**, *103*, 447-453.
74. Tang, Q.-L.; Chen, Z.-X. Density functional slab model studies of water adsorption on flat and stepped Cu surfaces. *Surf. Sci.* **2007**, *601*, 954-964.
75. Hughes, Z. E.; Wright, L. B.; Walsh, T. R. Biomolecular adsorption at aqueous silver interfaces: first-principles calculations, polarizable force-field simulations, and comparisons with gold. *Langmuir* **2013**, *29*, 13217-13229.
76. Drelich, J.; Chibowski, E.; Meng, D. D.; Terpilowski, K. Hydrophilic and superhydrophilic surfaces and materials. *Soft Matter* **2011**, *7*, 9804-9828.
77. Bernardin, J. D.; Mudawar, I.; Walsh, C. B.; Franses, E. I. Contact angle temperature dependence for water droplets on practical aluminum surfaces. *Int. J. Heat Mass Transfer* **1997**, *40*, 1017-1033.
78. Schrader, M. E. Wettability of clean metal surfaces. *J. Colloid Interface Sci.* **1984**, *100*, 372-380.
79. Trautvetter, M.; Wiedwald, U.; Paul, H.; Minkow, A.; Ziemann, P. Thermally driven solid-phase epitaxy of laser-ablated amorphous AlFe films on (0001)-oriented sapphire single crystals. *Appl. Phys. A* **2011**, *102*, 725-730.
80. Saraeva, I. N.; Kudryashov, S. I.; Rudenko, A. A.; Zhilnikova, M. I.; Ivanov, D. S.; Zayarny, D. A.; Simakin, A. V.; Ionin, A. A.; Garcia, M. E. Effect of fs/ps laser pulsewidth on ablation of metals and silicon in air and liquids, and on their nanoparticle yields. *Appl. Surf. Sci.* **2019**, *470*, 1018-1034.
81. Zhigilei, L. V.; Garrison, B. J. Microscopic mechanisms of laser ablation of organic solids in the thermal and stress confinement irradiation regimes. *J. Appl. Phys.* **2000**, *88*, 1281-1298.
82. Paltauf, G.; Dyer, P. E. Photomechanical processes and effects in ablation. *Chem. Rev.* **2003**, *103*, 487-518.
83. Leveugle, E.; Ivanov, D. S.; Zhigilei, L. V. Photomechanical spallation of molecular and metal targets: molecular dynamics study. *Appl. Phys. A* **2004**, *79*, 1643-1655.

84. Tsuji, T.; Thang, D.-H.; Okazaki, Y.; Nakanishi, M.; Tsuboi, Y.; Tsuji, M. Preparation of silver nanoparticles by laser ablation in polyvinylpyrrolidone solutions. *Appl. Surf. Sci.* **2008**, *254*, 5224-5230.
85. Hupfeld, T.; Laurens, G.; Merabia, S.; Barcikowski, S.; Gökce, B.; Amans, D. Dynamics of laser-induced cavitation bubbles at a solid–liquid interface in high viscosity and high capillary number regimes. *J. Appl. Phys.* **2020**, *127*, 044306.
86. Lasemi, N.; Pacher, U.; Zhigilei, L. V.; Bomati-Miguel, O.; Lahoz, R.; Kautek, W. Pulsed laser ablation and incubation of nickel, iron and tungsten in liquids and air. *Appl. Surf. Sci.* **2018**, *433*, 772-779.
87. Kwong, H. Y.; Wong, M. H.; Leung, C. W.; Wong, Y. W.; Wong, K. H. Formation of core/shell structured cobalt/carbon nanoparticles by pulsed laser ablation in toluene. *J. Appl. Phys.* **2010**, *108*, 034304.
88. Amendola, V.; Riello, P.; Meneghetti, M. Magnetic nanoparticles of iron carbide, iron oxide, iron@iron oxide, and metal iron synthesized by laser ablation in organic solvents. *J. Phys. Chem. C* **2011**, *115*, 5140-5146.
89. Marzun, G.; Boennemann, H.; Lehmann, C.; Spliethoff, B.; Weidenthaler, C.; Barcikowski, S. Role of dissolved and molecular oxygen on Cu and PtCu alloy particle structure during laser ablation synthesis in liquids. *Chem. Phys. Phys. Chem.* **2017**, *18*, 1175-1184.
90. Nadarajah, R.; Tahir, S.; Landers, J.; Koch, D.; Semisalova, A. S.; Wiemeler, J.; El-Zoka, A.; Kim, S.-H.; Utzat, D.; Möller, R.; *et al.* Controlling the oxidation of magnetic and electrically conductive solid-solution iron-rhodium nanoparticles synthesized by laser ablation in liquids. *Nanomaterials* **2020**, *10*, 2362.
91. Reich, S.; Göttlicher, J.; Ziefuss, A.; Streubel, R.; Letzel, A.; Menzel, A.; Mathon, O.; Pascarelli, S.; Baumbach, T.; Zuber, M.; *et al.* In situ speciation and spatial mapping of Zn products during pulsed laser ablation in liquids (PLAL) by combined synchrotron methods. *Nanoscale* **2020**, *12*, 14011-14020.
92. Kull, H. J. Theory of the Rayleigh-Taylor instability. *Phys. Rep.* **1991**, *206*, 197-325.
93. Thomas, D. A.; Lin, Z.; Zhigilei, L. V.; Gurevich, E. L.; Kittel, S.; Hergenröder, R. Atomistic modeling of femtosecond laser-induced melting and atomic mixing in Au film - Cu substrate system. *Appl. Surf. Sci.* **2009**, *255*, 9605-9612.
94. Qiu, T. Q.; Juhasz, T.; Suarez, C.; Bron, W. E.; Tien, C. L. Femtosecond laser heating of multi-layer metals - II. Experiments. *Int. J. Heat Mass Transfer* **1994**, *37*, 2799-2808.
95. Choi, G.-M.; Wilson, R. B.; Cahill, D. G. Indirect heating of Pt by short-pulse laser irradiation of Au in a nanoscale Pt/Au bilayer. *Phys. Rev. B* **2014**, *89*, 064307.
96. The equivalent diameter of a nanoparticle,  $D_e$ , is defined as  $D_e = \sqrt[3]{3N/2\pi a'}$ , where  $a' = a_{Ag}x_{Ag} + a_{Cu}x_{Cu}$ ,  $a_{Ag}$  and  $a_{Cu}$  are lattice parameters of Ag and Cu fcc crystals at 300 K, and  $x_{Ag}$  and  $x_{Cu}$  are molar fractions of Ag and Cu atoms in the nanoparticle.
97. Rouleau, C. M.; Shih, C.-Y.; Wu, C.; Zhigilei, L. V.; Puretzky, A. A.; Geohegan, D. B. Nanoparticle generation and transport resulting from femtosecond laser ablation of ultrathin metal films: Time-resolved measurements and molecular dynamics simulations. *Appl. Phys. Lett.* **2014**, *104*, 193106.
98. Vrij, A. Possible mechanism for the spontaneous rupture of thin, free liquid films. *Discuss. Faraday Soc.* **1966**, *42*, 23-33.
99. Ratautas, K.; Gedvilas, M.; Račiukaitis, G.; Grigonis, A. Nanoparticle formation after nanosecond-laser irradiation of thin gold films. *J. Appl. Phys.* **2012**, *112*, 013108.
100. Oh, H.; Pyatenko, A.; Lee, M. Laser dewetting behaviors of Ag and Au thin films on glass and Si substrates: Experiments and theoretical considerations. *Appl. Surf. Sci.* **2019**, *475*, 740-747.

101. Kondic, L.; González, A. G.; Diez, J. A.; Fowlkes, J. D.; Rack, P. Liquid-state dewetting of pulsed-laser-heated nanoscale metal films and other geometries. *Annu. Rev. Fluid Mech.* **2020**, *52*, 235-262.
102. Tamura, A.; Matsumoto, A.; Fukami, K.; Nishi, N.; Sakka, T. Simultaneous observation of nascent plasma and bubble induced by laser ablation in water with various pulse durations. *J. Appl. Phys.* **2015**, *117*, 173304.
103. Noack, J.; Vogel, A. Laser-induced plasma formation in water at nanosecond to femtosecond time scales: calculation of thresholds, absorption coefficients, and energy density. *IEEE J. Quantum. Electron.* **1999**, *35*, 1156-1167.
104. Waag, F. *Laser Synthesis of Metallic and Oxidic Transition Metal, Multi-Element Nanoparticles for Catalytic Applications*; Dissertation, University of Duisburg-Essen, 2019.
105. Atanasov, I.; Ferrando, R.; Johnston, R. L. Structure and solid solution properties of Cu–Ag nanoalloys. *J. Phys.: Condens. Matter* **2014**, *26*, 275301.
106. Dittrich, S.; Kohsawski, S.; Wittek, B.; Hengst, C.; Gökce, B.; Barcikowski, S.; Reichenberger, S. Increasing the size-selectivity in laser-based g/h liquid flow synthesis of Pt and PtPd nanoparticles for CO and NO oxidation in industrial automotive exhaust gas treatment benchmarking. *Nanomaterials* **2020**, *10*, 1582.

## Graphical Abstract

